Universiteit Utrecht

Frictional properties of simulated sandstone–coal fault gouge: Implications for seismicity in the Sydney basin and Groningen gas field

Milo Trainor Moss

MSc Thesis

Student number: 6509258

July 2021

First supervisor: Dr. André Niemeijer
Second supervisor: Prof. Dr. Martyn Drury

Abstract

Carbonaceous materials including amorphous carbon and graphite are observed in seismically active fault zones however their influence on the frictional properties of faults remains poorly understood. The Sydney basin in SE Australia contains extensive coal measures and networks of high angle faults which are susceptible to M_L= 5+ earthquakes. The structure of these faults is widely documented however the frictional properties have yet to be studied.

This study investigates the influence of coal on the frictional properties of sandstone hosted faults and in doing so contributes to the assessment of seismic hazard associated with faults in the Sydney basin. In addition, it also adds to our understanding of the faults which penetrate the coal bearing Carboniferous shale/siltstone under burden in the Groningen Gas field. Friction experiments were performed on simulated sandstone-coal fault gouge using samples of Coal Cliff sandstone and Illawarra coal collected from the Sydney basin. A combination of velocity stepping and constant velocity experiments were performed at 100 °C and effective normal stress of 40 MPa which are close to in situ conditions of the Groningen reservoir, using slip velocities from 0.1 – 10 μms^{-1}. Rate and state friction parameters (a-b) were derived, combined with X-ray microscopy, quantitative image analysis, SEM and Raman spectroscopy.

Both mixed sandstone-coal samples and the sandstone and coal end members displayed a μ_{peak} of ~0.43. Furthermore, the coal end member and coal rich samples (≥50 wt% coal) display intense post weakening before reaching a steady state of ~0.23, which is attributed to shear induced molecular change of coal. Upon shearing aromatic layers become more extensive as functional groups are omitted resulting in a structure closer to that of graphite. Despite both sandstone and coal end members displaying positive (a-b) values, coal rich sandstone-coal samples (≥50 wt% coal) are velocity weakening (negative a-b) at 1 and 10 μms^{-1} under water saturated conditions. The results indicate that sandstone hosted faults, which have been enriched with coal through smearing, may be susceptible to seismic slip under certain conditions.

Table of Contents

ABSTRACT 2

1 INTRODUCTION 5

1.1 Aim **7**

1.2 Theoretical background **7**
1.2.1 Shear zones 7
1.2.2 Rate and state friction theory 8
1.2.3 Coal molecular structure 10

2 METHOD 12

2.1 Sample material **12**

2.2 Friction experiments **13**
2.2.1 Sample preparation and assembly 13
2.2.2 Testing apparatus and procedure 14
2.2.3 Data acquisition and processing 16

2.3 Post-test analysis **19**
2.3.1 X-ray microscopy 19
2.3.2 SEM 21
2.3.3 Raman Spectroscopy 21

3 RESULTS 22

3.1 Mechanical Data **22**
3.1.1 Frictional strength – Velocity stepping experiments 22
3.1.2 Frictional strength – Constant velocity experiments 22
3.1.3 Velocity dependence of friction 23

3.2 Microstructure **26**
3.2.1 X-ray microscopy 27
3.2.2 Quantitative image analysis 29
3.2.3 SEM 32

3.3 Raman spectroscopy **35**

4 DISCUSSION 38

4.1 Frictional strength **38**
4.1.1 Coal Cliff Sandstone 38
4.1.2 Illawarra coal and mixed sandstone - coal gouge 39
4.1.3 Shear induced molecular change 40

4.2 Effect of coal on velocity dependence of friction **42**
4.2.1 Micromechanical framework of granular aggregates 42
4.2.2 Coal Cliff sandstone 43
4.2.3 Illawarra coal 44
4.2.4 Mixed sandstone – coal 45

4.2.5 Comparisons with previous work 46

4.3 Implications for seismicity in the Sydney basin and Groningen gas field **46**

5 RECOMMENDATIONS AND FUTURE RESEARCH 47

5.1 Improvements to microstructural analysis **47**

5.2 Future work **48**

6 CONCLUSIONS 49

7 ACKNOWLEDGEMENTS 50

REFERENCES 51

APPENDICES 57

A – Coal Cliff sandstone XRD **57**

B – Raman spectra **58**

1 Introduction

In the last 100 years there have been three major earthquakes in the Sydney basin region: M_L= 5.3 in 1925, M_L= 5.6 in 1989 and M_L= 5.3 in 1994. The largest of which occurred outside the city of Newcastle causing almost AU$ 200 million in damages and 13 fatalities (Figure 1A) (Rynn et al., 1992). Mass removal through coal mining was proposed by Klose (2007) as a possible cause for changes in the stress state of faults in the Sydney basin which consequently resulted in the 1989 Newcastle earthquake. However, in a discussion paper on the study Quinn et al (2008) argue that the author fails to provide convincing evidence to support this theory. However, they acknowledge that there is likely considerable horizontal stress anisotropy within the Sydney basin (Memarian and Fergusson, 2003). The present day stress field in the Sydney basin has a NNE to NE trending axis of maximum horizontal compressive stress however considerable local heterogeneity may exist due to geological structures (Hillis et al., 1999; Zhao & Müller, 2001). Increased compressive stress is widely observed in the flanks of folds and large fault zones which can influence the local stress field in both magnitude and orientation (Burra et al., 2014; Rajabi et al., 2016; Taghipour et al., 2019). Similarly, changes in rock properties due to variations in strata can have a considerable impact on the stress distribution (Peacock & Sanderson, 1992). Furthermore, the need to understand the stability of faults and reactivation mechanisms in the Sydney region has become more pressing with the discovery that the Lucas Heights nuclear reactor outside Sydney is built on a fault zone. In addition, the impact of a large M_L= ~5 earthquake on Sydney which has a population of 5.4 million would be catastrophic (Australian Bureau of Statistics, 2021).

The Sydney basin is a foreland basin consisting of an Early Permian to Middle Triassic succession of sedimentary and igneous rocks (Figure 1B). The basin originally developed under a convergent tectonic regime associated with subduction along the southernmost margin of Gondwana. The Triassic succession is subdivided into three groups, the Wianamatta Group, the Hawkesbury sandstone and the Narrabeen group, the latter of which overlays Upper Permian Illawarra coal measures (Figure 1B). The Coal Cliff sandstone is located at the base of the Narrabeen group and forms an erosional contact with the Bulli seam (Illawarra coal). It has an average thickness of ~15.0 m and contains mudstone, siltstone and sandstone facies, the latter of which is the most dominant. Bedding is thin to massive and mudstone clasts and rare pebbles are observed in the facies in the lower part of the formation. There is also an abundance of clay minerals including mixed illite-smectite and kaolinite (Al-Kahtany and Al Gahtani, 2015; Grevenitz et al., 2003; McLoughlin et al., 2021). Coal samples used in this study were collected from the Bulli seam which has a thickness of 2–3 m and is composed of well banded medium volatile bituminous coal (Figure 1B). Minor mineral assemblages are also present including quartz, kaolinite and carbonates. Permian coal seams are interbedded with minor carbonaceous mudstone interbeds, conglomeratic sandstones and tuff layers. (Jones et al., 1987; Bamberry, 1991; Zhao et al., 2013). Four major NNE striking fault zones (Watsons Bay Fault zone, Woolloomooloo Fault zone, Luna Park Fault zone and Homebush Bay Fault zone) have been identified within the Triassic sandstone groups which include a combination of well exposed strike slip, normal and reverse faults (Memarian and Fergusson, 2003; Och et al., 2009). Furthermore, syn-depositional folding has exposed Permian Illawarra coal measures at or near the surface reaching a maximum thickness of ~500 m in the north of the southern coal field (Figure 1A).

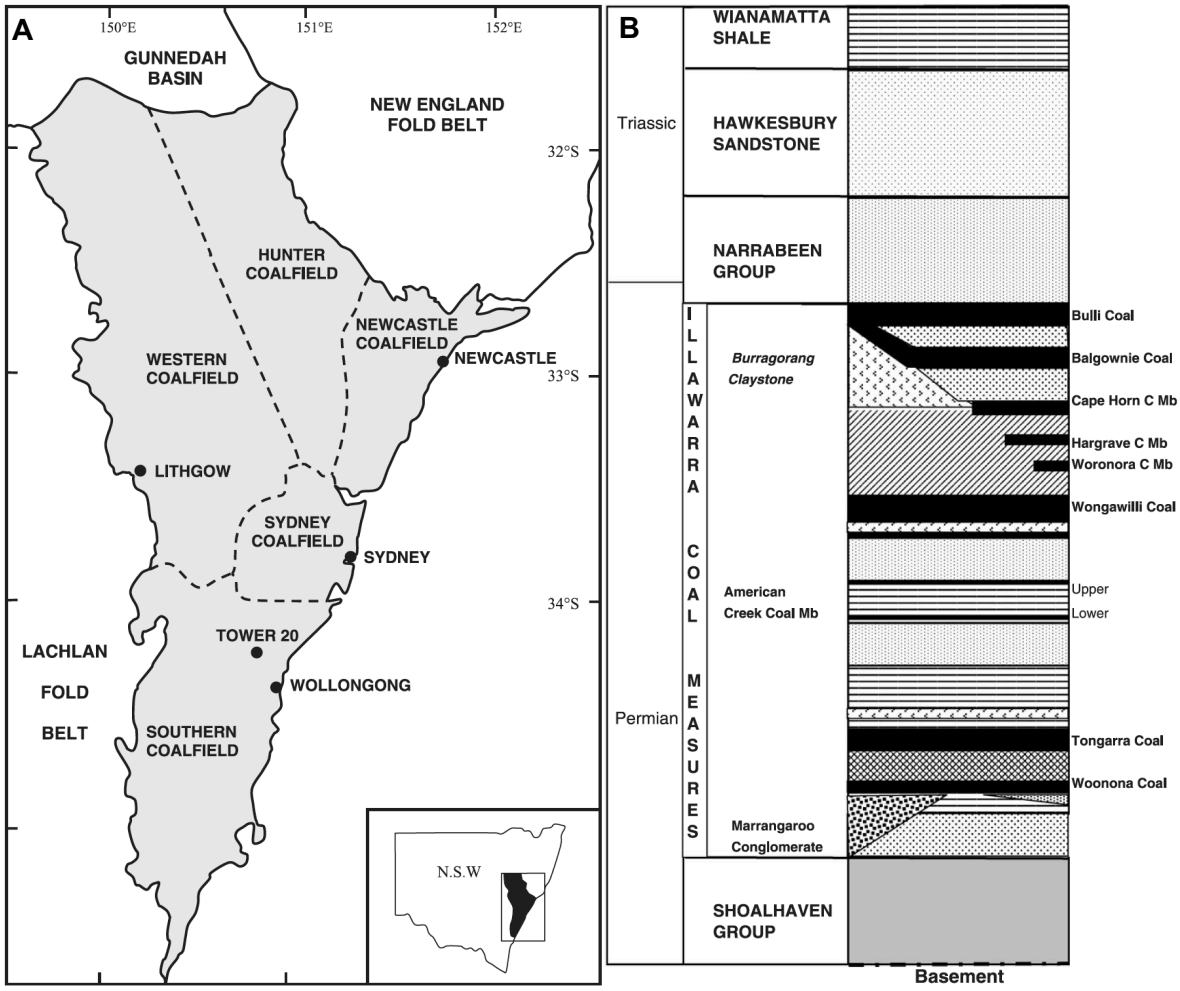

Figure 1: Location map and stratigraphic sequence of the Sydney basin (Grevenitz et al., 2003). Samples used in the friction experiments were collected from an outcrop outside of Wollongong (34° 15' 20" S 150° 58' 22" E). (b) The Coal Cliff sandstone is found at the base of the Narrabeen group and has an erosional contact with the Bulli coal seam below.

Weak phase materials (talc, clay, amorphous carbon and graphite) have been widely observed in the fault gouge of major seismically active faults zones such as the San Andreas in the USA (Moore and Rymer, 2007), the Alpine Fault in New Zealand (Schleicher et al., 2015) and the Atotsugawa fault system in Japan (Oohashi et al., 2012). Furthermore, experimental studies have demonstrated that they can have a disproportionately large impact on fault friction relative to the volume present, depending on their spatial distribution (Collettini et al., 2009; Tembe et al., 2010). Fault friction and stability is controlled by complex interactions between multiple mechanical and physical factors including state of stress, mineral composition and hydraulic properties (Rutter et al., 2013). As such it is necessary to conduct field specific studies which focus on the stability of faults under in situ conditions. Studies on the influence of coal on frictional properties of faults under in situ conditions remain limited with the only recent contribution from Liu et al. (2020) who investigated the impact of coal on faults in the Carboniferous shale under burden of the Groningen Gas field in the Netherlands. Although not tectonically active, the Groningen gas field has experienced recent seismicity which has progressively increased in intensity and magnitude from 2003 to 2014 (Van Thienen-Visser and Breunese, 2015). The induced seismicity has been attributed to

compaction at reservoir depth resulting in stress changes and reactivation of pre-existing faults (NAM, 2013; Buijze et al., 2017). Much of the research to date has focused on deformation in the Slochteren sandstone reservoir rock and reactivation of faults which incise the reservoir. However, there is diverse array of faults which penetrate both the under burden and the reservoir which remain poorly understood (Kortekaas and Jaarsma, 2017).

Friction experiments performed by Liu et al., (2020) using Carboniferous Limburg shale/ siltstone-coal simulated fault gouge at in situ conditions of the reservoir (P_c = 55 MPa, P_p = 15 MPa and T = 100°C) observed intense displacement dependent weakening in coal rich samples. However, they found that, certainly from a rate and state (RSF) point of view, the presence of coal would not promote earthquake nucleation on faults in the Limburg shale/ siltstone unit. Experiments performed by Oohashi et al. (2011) and Fan et al. (2020) both reported a shear induced increase in the crystallinity of amorphous carbon and coal respectively which could explain the intense weakening trend observed in coal rich samples. Furthermore, smearing of coal into weak zones combined with the low frictional strength of carbonaceous materials (graphite and amorphous carbon) may have a lubricating effect. However, the mechanism which leads to this increase in crystallinity and its impact on strain localisation is still unclear. In addition, the influence of coal on the frictional properties of sandstone fault gouge has yet to be investigated.

1.1 Aim

Employing a similar approach as Liu et al. (2020) but using samples of Coal Cliff sandstone and Illawarra coal, I investigated the influence of coal on sandstone bearing faults in the Sydney basin. RSF parameters for sandstone-coal simulated fault gouge were derived, with varying coal content from 0-100 wt%. Constant velocity experiments were also performed, combined with XCT (X-ray computed tomography) and quantitative image analysis to measure how coal distribution within the gouge evolves with shear. This was combined with SEM and Raman spectroscopy to investigate the mechanisms controlling friction and shear induced crystallinity change in carbon. In doing so we aim to contribute to the assessment of the seismic hazard of faults in the Sydney basin. Furthermore, this study will build on the findings of Liu et al. (2020) and contribute to a clearer understanding on the seismic potential of faults in the Groningen gas field.

1.2 Theoretical background

1.2.1 Shear zones

Shear zones display a specific array of structures or Riedel shears which can be observed from a micro to crustal scale. An idealised Riedel shear geometry consists of synthetic Riedel shears (R_1), antithetic/conjugate Riedel shears (R_2) and secondary synthetic shears (P) with respect to the principal slip zone or Y shear. Numerous authors have observed these structures in clay cake experiments (Tchalenko, 1970) shear box experiments (Mandl; 1977) and triaxial experiments (Marone and Scholz, 1989; Logan et al. 1992). They demonstrate that the structures develop with increasing shear strain and correspond to different stages of the shear stress-displacement curve. Logan et al., (1992) provides an in-depth classification for these structures in simulated fault gouge outlined below and visually represented in Figure 2.

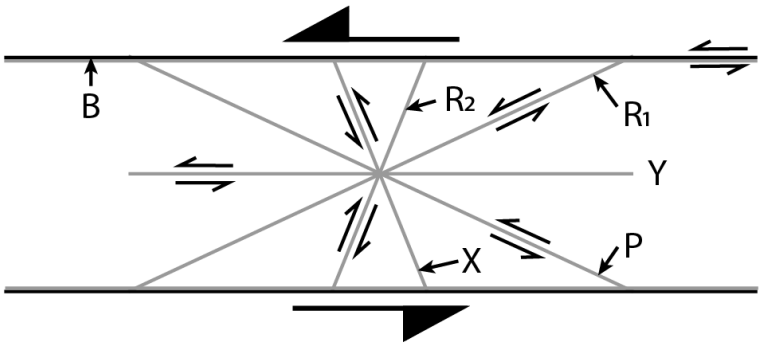

Figure 2: Schematic illustration of structural elements in simulated fault gouge according to Logan et al. (1979).

R_1 shears are the first to occur and start to develop at or close to peak strength. They are discontinuous and do not extend across the entire thickness of the gouge. Post peak strength, continuous R_1 shears extend across the gouge layer and R_2 shears form at high angles to the driver block. With increasing shear displacement R_1 shears rotate to form boundary parallel Y-shears and incipient P shears also start to develop. P-shears then extend across the thickness of the gouge as it approaches steady state sliding. At steady state a continuous through going Y-shears accommodates almost all the displacement within the gouge. The Y or B shear commonly develops along or close to the gouge - driver block interface (Figure 2). Although this geometrical array of structures has been produced in a variety of materials under a broad range of experimental conditions (confining pressure, pore pressure, temperature and slip velocity) material properties can have a considerable impact on their development. For example, weak phase materials often promote localisation and the development of a through going foliation (Tembe et al., 2010).

1.2.2 Rate and state friction theory

The movement of tectonic plates results in the build-up of elastic energy in the material around a fault. This increases the shear stress along the fault until the shear strength is reached which triggers slip. The frictional strength is dependent on the true contact area of the surfaces and the shear strength of the contacts or asperities. For slip to occur asperities must fracture or deform which cost energy. Hence the surface roughness and properties of asperities are crucial for controlling fault slip. Slip on faults can be represented using a simple spring-slider model (Figure 3). In natural faults N is the normal load on the fault plane F is the frictional strength of the fault, k is the elasticity of the surrounding rock mass and v is the velocity of plate motion. In rock friction experiments N is the normal load on the sample F is the frictional strength, k represents the elastic properties of the apparatus and v is slip velocity. Assuming that the spring is linear elastic and velocity is constant, shear stress will increase as the block is pulled. As the block moves, stress drops and the spring compresses and movement stops. Once movement stops the frictional strength of the surface is recovered and the process repeats. This repeating process is known as stick-slips which are considered to be the laboratory representation of earthquakes (Scholz, 2019).

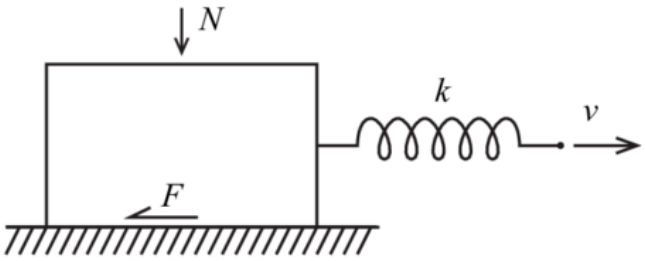

Figure 3: Spring slider model for origin of a slip instability. The slider and the surface have a static friction *F* which resists slip. The spring is pulled at velocity *v* until the frictional strength is exceeded at which point the slider will move to the right. The elastic energy is converted to kinetic energy and the spring retracts.

The frictional behaviour of faults can be fitted using the rate and state friction law (RSF) shown in equation 1. This commonly used method describes the rate dependence of friction of a given material and hence provides an indication of its seismic potential. RSF provides a relationship between measured coefficient of friction (μ), rate of deformation (*V*) and state (θ). The most widely used form is (Dieterich, 1979; Ruina, 1983):

$$\mu = \mu_0 + aln\left(\frac{V}{V_0}\right) + bln\left(\frac{V_0\theta}{d_c}\right) \qquad (1)$$

where, μ is the coefficient of friction and μ_0 is the coefficient of friction at a reference velocity V_0. Parameters *a* and *b* are constants that describe the instantaneous 'direct' effect and the time-dependent 'evolution' effect respectively and together represent the material properties of the gouge. In the formulation *a* can be interpreted as the influence of loading rate on asperity contact strength and *b* as the change in asperity contact area and intrinsic strength due to change in the lifetime of asperity contact (Niemeijer et al., 2010). d_c is the critical slip distance over which the state variable evolves to a new steady state. Figure 4A visually represents this relationship. The state variable is thought to represent the average lifetime of grain scale asperity contacts and is described with the Dietrich or 'ageing' law:

$$\frac{d\theta}{dt} = 1 - \frac{V\theta}{d_c} \qquad (2)$$

This accounts for the fact that real contact area is time dependent as shearing breaks the surfaces that are in contact, decreasing the contact area. To account for the elastic response of the apparatus equations 1 and 2 are solved in conjunction with the following equation:

$$\frac{d\mu}{dt} = k\left(V_{lp} - V\right) \qquad (3)$$

where k is the stiffness of the apparatus, V_{lp} is the load point velocity and *V* is the true slip velocity. Once steady state is reached equation 1 reduces to:

$$(a-b) = \frac{\mu-\mu_0}{ln^{V}/_{V_0}} \qquad (4)$$

Where $(a-b)$ is the rate sensitivity parameter. A positive (a-b) value indicates velocity strengthening, in other words, friction will increase with a stepwise change in slip velocity. Conversely negative (a-b) values indicate velocity weakening characteristics. Ruina (1983) demonstrated that a material which exhibits negative (a-b) values is susceptible to stick-slip behaviour and therefore it is assumed that seismogenic faults exhibit a negative (a-b) (Van den Ende et al., 2018).

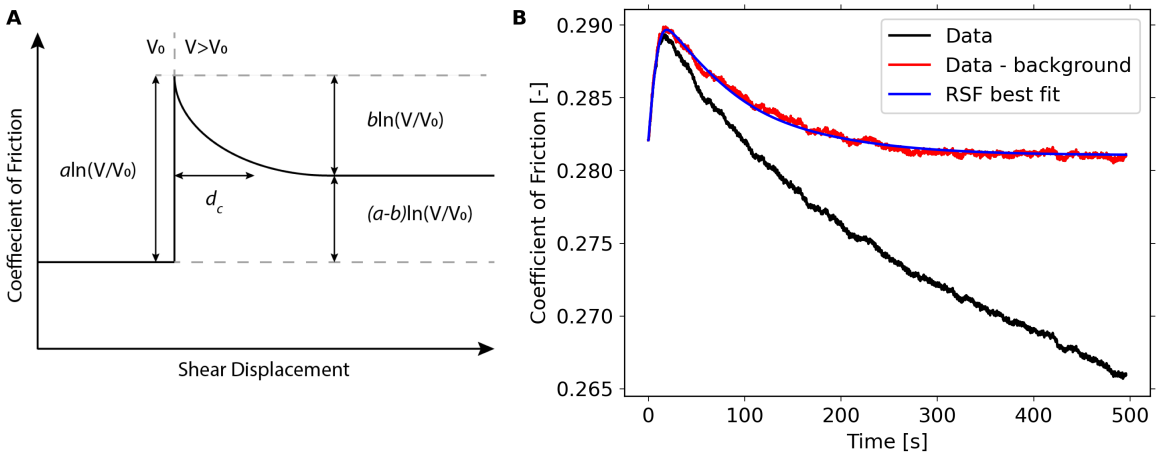

Figure 4: (a) Effect on friction of an instantaneous increase in slip velocity. V_0= initial slip velocity, V = new slip velocity. *a*ln(V/V_0) or 'direct effect' is the instantaneous change in friction caused by the change in velocity. *b*ln(V/V_0) or 'evolution effect' is the change in friction to a new steady state value over a distance d_c (critical slip distance). (b) Example of RSF law fitted to velocity step from 0.1 – 1 μms^{-1} in experiment s023 (50 wt% coal) with background weakening trend removed.

Returning to the spring-slider model for slip on a fault. The system is stable if the stiffness of the system is higher than the stiffness of the fault:

$$k > k_c = -\frac{\sigma_n^{eff}(a-b)}{d_c}$$

in which *k* is the stiffness of the system, k_c is the critical stiffness and σ_n^{eff} is the effective normal stress (Tanner and Brandes, 2020). Stick slips only occur in the velocity weakening regime (negative a-b), in other words when friction decreases with increasing velocity. In this regime friction must decrease faster than the rate of elastic unloading of the spring (Figure 3). Nevertheless, extrapolation of laboratory derived RSF parameters to natural faults must be done with caution as the natural faults will likely experience much larger velocity increases at nucleation than those achieved in the laboratory (Ampuero and Rubin, 2008).

1.2.3 Coal molecular structure

In simple terms the molecular structure of coal consists of aromatic layers composed of aromatic rings surrounded by peripheral aliphatic chains and functional groups (Mathews and Chaffee, 2012). The general classifications for coal with increasing rank are: lignite, sub-bituminous, bituminous and anthracite. Molecular structure evolves during the coalification process, with increasing rank aliphatic chains and functional groups are progressively removed and the aromatic rings are condensed forming more extensive aromatic layers. This

process is schematically illustrated in Figure 5 (Ghani et al., 2015; Hou et al., 2017). The aliphatic chains are composed of hydrocarbons while the majority of the functional groups contain oxygen. However, the macromolecular structure of coal is composed of three-dimensional networks resulting in considerably heterogeneity in the structure. Hence it is difficult the characterize.

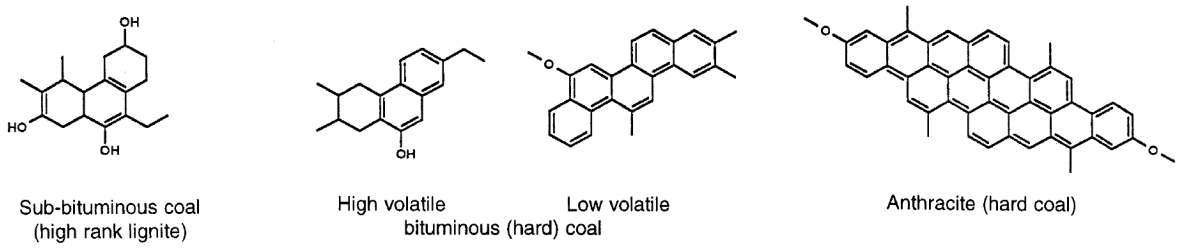

Figure 5: Molecular structure of coal (Fakoussa and Hofrichter, 1999). Increasing coal rank from left to right.

1.2.4 Raman spectra of Carbon

The Raman spectrum of carbonaceous material is highly sensitive to structural ordering hence it provides reliable information on how the molecular structure of coal evolves during the coalification process. The Raman spectra of disorder Carbon contains a first order (1000 – 1800 cm^{-1}) and second order region (2400 – 3500 cm^{-1}). The first order region contains two distinct peaks, the G peak around 1580–1600 cm^{-1} and the D peak at ~1350 cm^{-1} shown in Figure 6A (Fischbach and Couzi, 1986; Ferrari and Robertson, 2000). Graphite consists of sp^2 carbon hexagonal networks of carbon atoms which are covalently bonded in plane and have weak van der Waals interaction between planes. The G peak corresponds to the in plane stretching vibration of double carbon atom bonds with E_{2g2} symmetry (Trusovas et al., 2015). The D band, which is associated with structural defects and heterogeneities relates to the breathing mode between aromatic rings with a A_{1g} symmetry, shown in Figure 6B (Pimenta et al., 2007; Chacón-Torres et al., 2012). In coal the intensity ratio of the D and G peaks $\left(\frac{ID}{IG}\right)$ and the position of the D and G peaks are the most widely used parameters to characterise crystallinity. In addition, $\left(\frac{ID}{IG}\right)$ is also used to estimate the lateral size of in plane crystallites (L_a). As outlined in section 1.2.3, during the coalification process the size of the aromatic layers increases and structural ordering improves resulting in a molecular structure closer to that of a graphite structure. This change is reflected in the Raman parameters, as coal rank increases the position of the G peak moves to higher frequency whereas the position of the D peak shifts to lower frequencies. $\left(\frac{ID}{IG}\right)$ decreases as the structure becomes more ordered and consequently L_a increases as the size of the aromatic layers increases (He et al., 2017; Jiang et al., 2019).

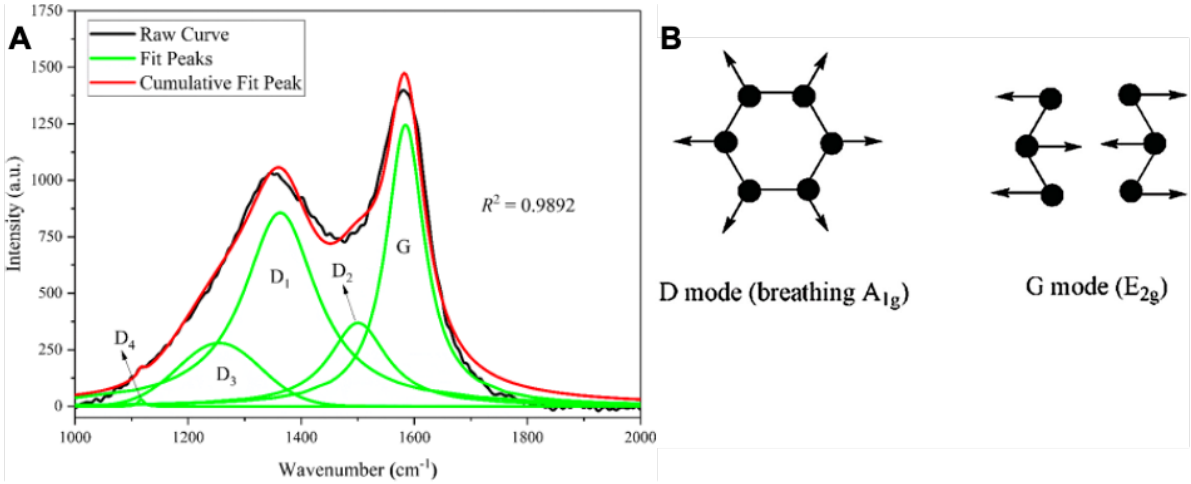

Figure 6: Raman spectroscopy of disordered Carbon. (a) Raman spectra with four Lorentz peak (D_1, D_2, D_4 and G) and one Gaussian peak (D_3) (Jiang et al., 2019). (b) Vibration modes of carbon atoms (Trusovas et al., 2015).

2 Method

2.1 Sample material

The simulated fault gouge used in the experiments was prepared using samples of Coal Cliff sandstone and Illawarra coal (Bulli seam) collected from the Southern Sydney basin (Figure 1A). XRD analysis and peak fitting using Match! software of the Coal Cliff sandstone gave a composition of 53.5 wt% Quartz, 44.1 wt% clay minerals with minor amounts of Feldspar (1.8 wt%), Pyrite (0.3 wt%) and Calcite (0.2 wt%) (Brandenburg and Putz, n.d.). Kaolinite is the dominant clay mineral (34.4 wt%) with minor amounts of Siderite, Chlorite and Illite, see Table 1 for details and Appendix A for spectra.

Table 1: XRD composition of Coal Cliff sandstone. All compositions in wt%.

Mineral	**Content** [wt%]
Quartz	53.5
Kaolinite	34.4
Siderite	5.3
Chlorite	2.9
Feldspar	1.8
Illite	1.5
Pyrite	0.3
Calcite	0.2

Analysis performed by Day et al. (2008) on 10 samples of Illawarra coal from the Sydney basin indicates that it can be classified as high to medium volatile bituminous coal. It has an average vitrinite reflectance of 0.77 – 1.27% and average vitrinite content of 60.99%, Liptinite of 2.44% and Inertinite of 36.56%. The samples contain 85.80 wt% Carbon, 5.13 wt% Hydrogen and Nitrogen 1.91 wt%. Grain size analysis was performed on the starting Illawarra coal and Coal

Cliff sandstone end members, the results of which are displayed in Figure 7. The mean initial grain size of the Illawarra coal is 27.44 μm and 20.01μm for the Coal Cliff sandstone.

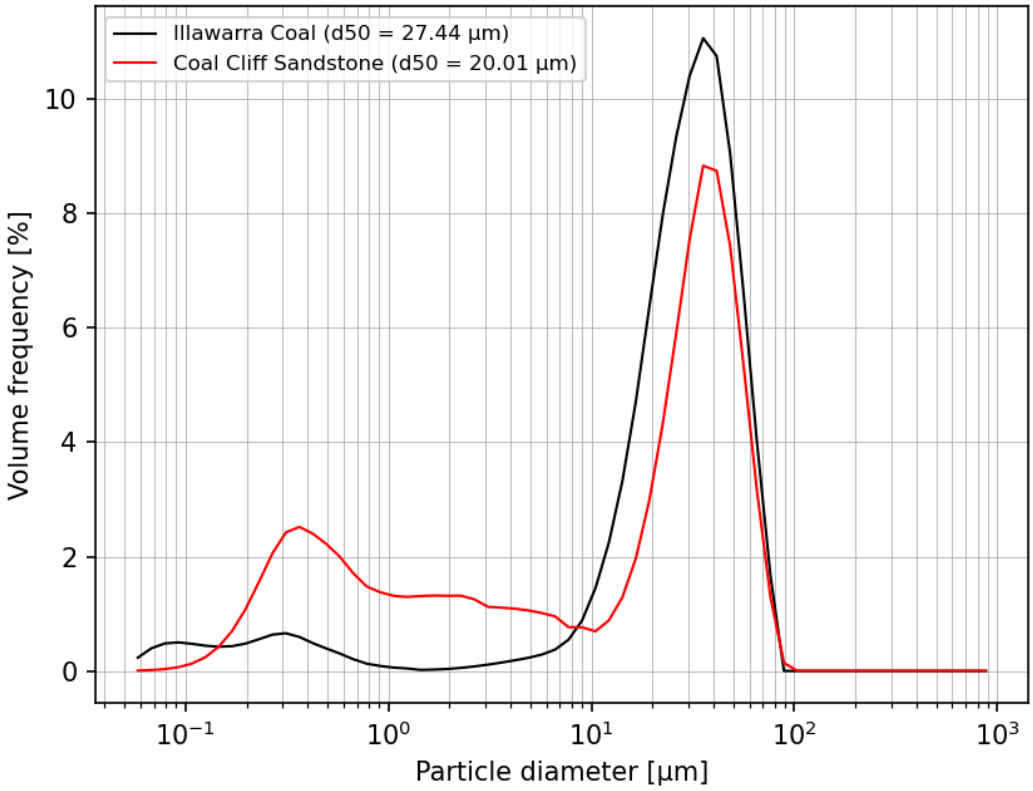

Figure 7: Grain size plot of end member materials used in friction experiments. Measurements taken using a laser particle analyser.

XRD analysis performed by Hunfield et al. (2017) on Slochteren sandstone showed that Quartz is the dominant phase (83 wt% below GWC) with only minor amounts of Feldspar (4 wt%) and clay (6 wt% Kaolinite and phengite). This is a significant difference in composition compared to the Coal Cliff sandstone, in particular in the Quartz and Kaolinite content.

2.2 Friction experiments

2.2.1 Sample preparation and assembly

To prepare the gouge, Coal Cliff sandstone and Illawarra coal samples were crushed with a mortar and pestle and sieved to a grain size of <50 μm. Samples were prepared for direct shear testing using two opposing cylindrical L-shaped steel pistons, dimensions 46 x 35 x 3 mm. The sample is sandwiched between two porous steel aggregate plates with pre-cut 0.05 mm grooves that grip the sample (Figure 9C).

The piston was first secured in a purpose-built jig with a semi-cylinder plastic spacer and then 3.2 g of gouge was evenly distributed over the porous plate (Figure 8A). The percentage of end members (Coal Cliff sandstone and Illawarra coal) was varied in wt% from 0-100 wt% in 25 wt% increments. To ensure homogeneous mixing of the starting gouge the end members were first mixed in a flat-bottomed dish using a razor blade. The mixed gouge was then spread evenly across the porous plate and a steel block was placed on top of the gouge. The sample

was then compacted using a pneumatic press for 1 minute at 35 kN rotating the jig after 30 seconds to ensure an even thickness of the gouge, creating a thin wafer ~1.1 mm thick. The piston was then carefully removed from the jig and corresponding L-shaped piston and porous plate were placed on top of the sample. The two pistons were then encased in a tube of FEP (Fluorinated Ethylene Propylene) heat shrink to support the assembly. Half disks of Ecoflex wrapped in PTFE (polytetrafluorethylene) sheet were inserted into the displacement accommodating cavities and held in place with Teflon tape (Figure 8B). As the Ecoflex is heated it fills the cavities and is easily extruded as the cavities close due to shortening. The piston assembly was then connected to the upper and lower forcing blocks using an additional FEP tube which was sealed using steel wire tourniquets (Figure 9A). In addition, a thin PTFE sheet was inserted between the pistons and forcing blocks to eliminate the effect of friction.

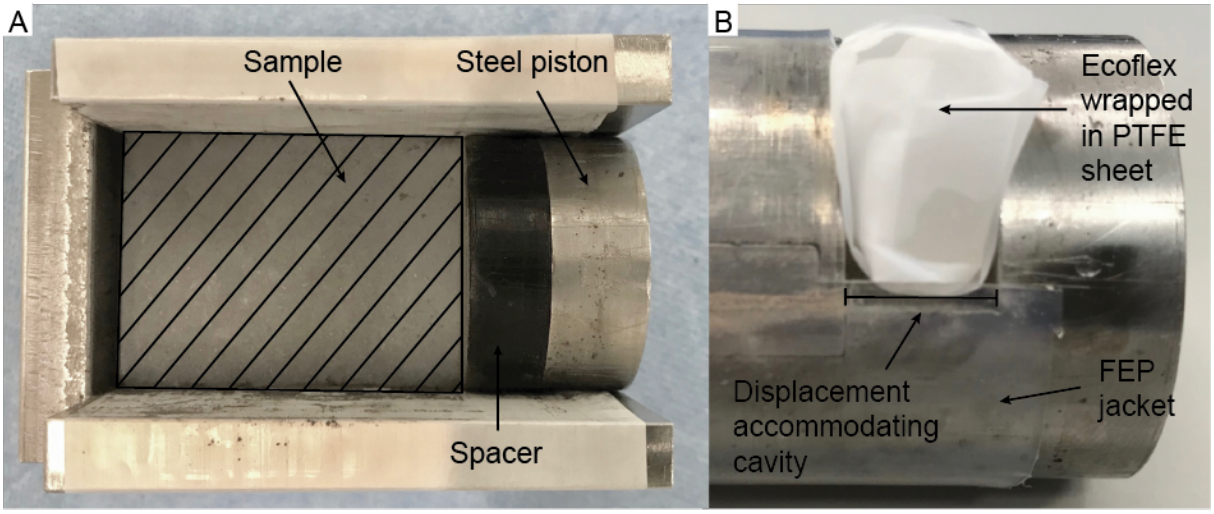

Figure 8: Images of piston assembly components. (a) preparation jig with pistons and sample. (b) Eco flex spacer wrapped in PTFE sheet.

2.2.2 Testing apparatus and procedure

The deformation apparatus used in the following experiments is a constant volume silicon-oil triaxial deformation apparatus mounted within an electronically servo-controlled Instron loading frame. A schematic cross section is provided in Figure 9 from Liu et al. (2020) (modified after Verberne et al. (2014)).

Confining pressure is achieved using a compressed air driven diaphragm pump and then maintained at desired conditions using a ISCO 65D servo-controlled syringe pump (control accuracy of ± 0.05 MPa). Pore fluid pressure is generated and then maintained at a constant pressure with a second ISCO 65D syringe pump. The pressure vessel is internally heated using a thermocoax furnace which can be controlled to within 0.1°C. Furthermore, temperature is measured with an inconel-sheathed, k-type thermocouple in a hole drilled in the pistons 5 mm from the sample (Figure 9A). Axial load is applied using an Instron 1362 electro-servo-controlled loading frame and the displacement is measured externally with a LVDT (linear variable differential transformer) which has an accuracy of ± 1.5 μm. The force is measured internally and therefore devoid of seal friction, using a DVRT (differential variable reluctance transformer) (± 33 N resolution).

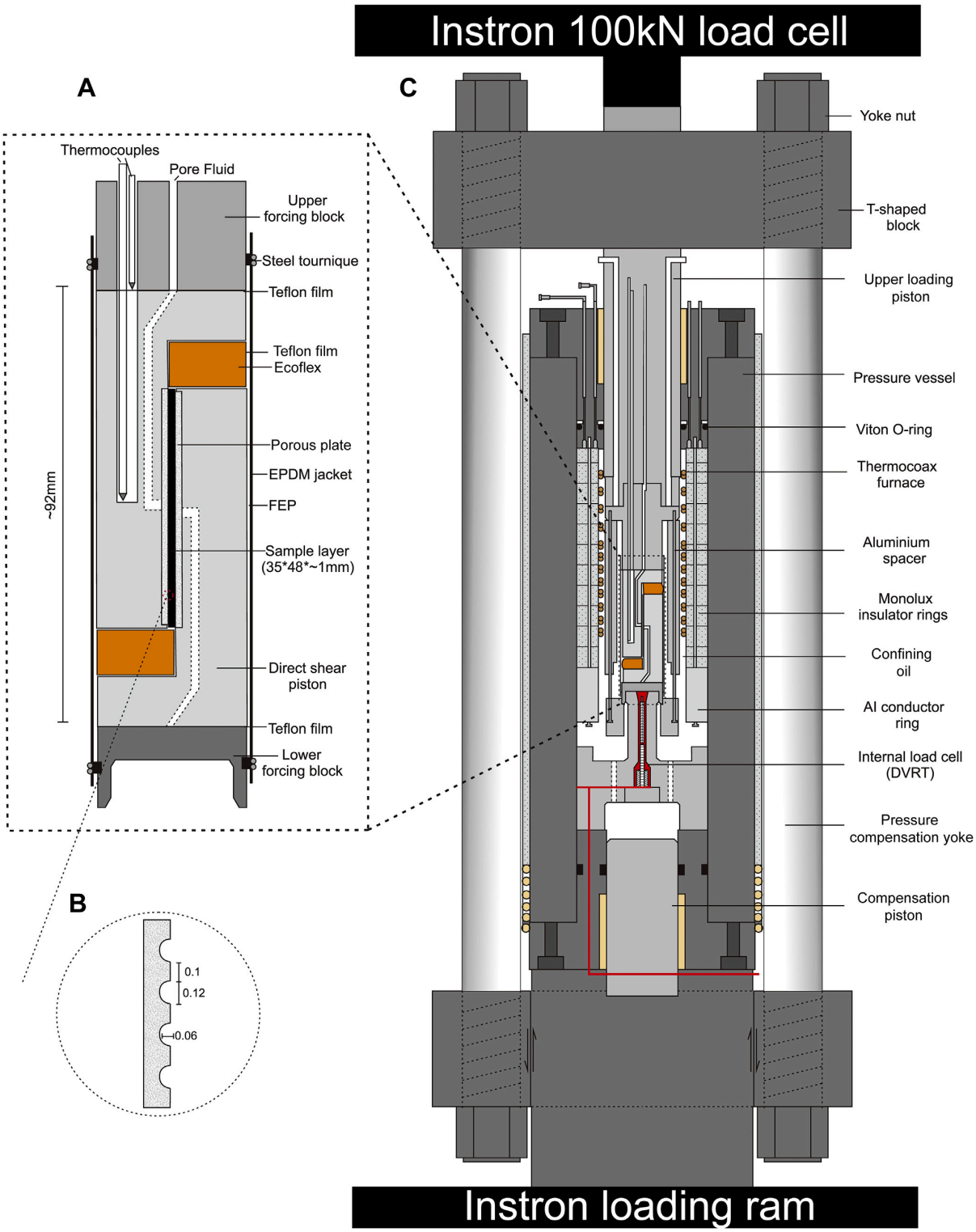

Figure 9: Schematic cross section of Triaxial direct shear deformation apparatus (Liu et al., 2020, modified from Verberne et al., 2014 original). (a) direct shear 'shuttle' sample assembly. (b) porous steel plate with machined groves to grip the sample. (c) Triaxial direct-shear deformation apparatus.

All experiments carried out in the following study were performed at a confining pressure of 55 MPa and pore fluid pressure of 15 MPa resulting in an effective normal stress imposed on the sample of 40 MPa. Deionised water was used for pore fluid in all of the experiments. Furthermore, experiments were performed at ~100 ºC to obtain conditions close to in situ conditions of the Slochteren sandstone reservoir, see Table 2 for full details of experimental conditions. Confining pressure, pore fluid pressure and temperature were increased in increments until the desired conditions were reached, the sample was then left to equilibrate overnight. To begin shearing the Instron loading ram was run at a constant velocity of 1 μms^{-1} until a touch point was reached. This was denoted by an abrupt increase in the internal load and indicates the start of loading of the sample. Both 'velocity stepping' (VS) and 'constant velocity' (CV) procedures were employed. In the former the experiment was run at a velocity of 1 μms^{-1} for ~1.5 – 2 mm by which point the peak strength of the sample had been achieved. Slip velocity was then changed in a stepwise manner from 0.1-10 μms^{-1} (1->0.1->1->10->1->10->1->10) with displacement intervals of ~0.3 – 0.7 mm to achieve a cumulative displacement of ~5.5 mm. All constant velocity experiments were performed at a constant velocity of 1 μms^{-1} to varying displacements (Table 2). To terminate the experiments the loading ram was retracted until there was no axial load on the sample. Confining pressure, pore fluid pressure and temperature were then decreased in increments to atmospheric conditions. Once the sample was removed from the deformation apparatus, the forcing blocks were disassembled, and piston assembly was dried for 3-4 days in an oven at 50ºC.

2.2.3 Data acquisition and processing

Axial load, axial displacement, confining pressure, pore fluid pressure and temperature were all recorded using a National Instruments 16-bit A/D data acquisition system and custom VI logger software at a logging rate of 10 Hz. The data reduction procedure outlined in Hunfield et al. (2017), was used to calculate shear displacement of the sample, shear stress (τ), effective normal stress $\left(\sigma_n^{eff}\right)$ and coefficient of friction (μ). Corrections are made to account for variations in confining pressure (P_c) which affects the internal load cell measurement:

$$F_{int[kN]} = F_{int[V]} \times \left(\left(P_{c[MPa]} \times A\right) + B\right) \qquad (5)$$

where $F_{int[kN]}$ is the corrected axial load, $F_{int[V]}$ is the measured internal load, *A* describes the sensitivity of the internal load cell to fluctuations in confining pressure and *B* is the conversion parameters for Volts to kN. Shear displacement is corrected to account for machine distortion of the deformation apparatus using an 8th order polynomial:

$$Machine\ distortion_{[mm]} = a\left(F_{int[kN[}\right)^8 + b\left(F_{int[kN[}\right)^7 + c\left(F_{int[kN[}\right)^6 \cdots + i\left(F_{int[kN[}\right)^0 \qquad (6)$$

parameters a-i are obtained from calibrations runs on a steel dummy of known elastic properties. The sample area is assumed to be constant throughout the experiment, so shear stress is calculated by dividing axial force by 1,610 mm^2 (area of porous plate). Assuming zero cohesion, the apparent coefficient of friction is the ratio of shear stress over effective normal stress,

$$\mu = \frac{\tau}{\left(\sigma_n^{eff}\right)} \qquad (7)$$

in which $\sigma_n^{eff} = \left(P_c - P_f\right)$.

The rate dependence of friction was quantified using Rate and state friction theory (RSF) which is outlined in section 1.2.2. RSF parameters, *a*, *b* and d_c were then calculated by fitting the processed friction data for each velocity step using an inverse modelling technique similar to the approach outlined in Blanpied et al. (1998). The inversion is performed by simultaneously solving equations 2 and 3 with equation 1 as a constraint. In this study two state variables were used to represent the evolution of friction so equation 1 is rewritten in the below form:

$$\mu = \mu_0 + aln\left(\frac{V}{V_0}\right) + b_1 ln\left(\frac{V_0\theta_1}{d_{c1}}\right) + b_2 ln\left(\frac{V_0\theta_2}{d_{c2}}\right) \qquad (8)$$

The six constitutive parameters (*a, b_1, b_2, d_{c1}* and *d_{c2}*) are then obtained as a solution to the non-linear inverse problem using an iterative least square method to fit the parameters of the forward model to the data. This was performed using the PyRSF modelling tool and is graphically illustrated in Figure 4B. Prior to fitting, background displacement weakening and strengthening trends were removed.

Table 2: Sample conditions and key mechanical data. VS = velocity stepping, CV = constant velocity, CCS = Coal Cliff Sandstone, SS = Slochteren Sandstone, C = Coal, Pc = confining pressure, Pf = pore fluid pressure, T = temperature, DI-water = deionised water, Dtot = total shear displacement, μ_{peak} = peak friction coefficient, μ_1 = friction coefficient at the start of the velocity stepping sequence, μ_{ss} = steady state or final friction coefficient i.e. steady state is not reached. * Friction data from Hunfield et al. (2017).

Experiment	Experiment type	Gouge composition [wt%]	Pc [MPa]	Pf [MPa]	T [oC]	Pore fluid	Slip velocity [μms^{-1}]	D_{tot} [mm]	μ_{peak} [-]	μ_1 [-]	μ_{ss} [-]
s021	VS	HS	55	15	100	DI-water	0.1 - 10	5.897	0.425	0.387	0.313
s022	VS	75:25 CCS:C	55	15	100	DI-water	0.1 - 10	5.313	0.432	0.333	0.310
s023	VS	50:50 CCS:C	55	15	100	DI-water	0.1 - 10	5.747	0.409	0.296	0.224
s026	VS	25:75 CCS:C	55	15	100	DI-water	0.1 - 10	4.134	0.458	0.304	0.231
s027	VS	C	55	15	100	DI-water	0.1 - 10	4.218	0.419	0.293	0.245
s033	CV	75:25 SS:C	55	15	100	DI-water	1	5.612	0.573	N/A	0.509
s031	CV	50:50 CCS:C	55	15	100	DI-water	1	5.161	0.451	N/A	0.231
s040	CV	75:25 CCS:C	55	15	100	DI-water	1	4.919	0.452	N/A	0.372
s041	CV	50:50 CCS:C	55	15	100	DI-water	1	1.948	0.434	N/A	0.245
s042	CV	75:25 CCS:C	55	15	100	DI-water	1	1.500	0.428	N/A	0.407
S1SSG-02*	VS	SS	55	15	100	DI-water	0.1 – 10	5.49	0.616	0.611	0.608

2.3 Post-test analysis

Following drying of the sample assembly for 3-4 days, the sample was removed and then preserved in Araldite 20/20 Epoxy resin. Microstructural analysis was then performed on four samples, s031, s040, s041 and s042 using a combination of XCT (X-ray Computed Tomography) analysis and SEM. In addition, Raman spectroscopy was carried out to characterize the molecular structure of the coal.

2.3.1 X-ray microscopy

To investigate the 3D structure and coal distribution within the deformed gouge, XCT was performed on a ~5 mm wide section cut parallel to the shear direction, using a Zeiss Xradia 610 Versa microscope. A representative volume with dimensions 14 x 3.5 x 3.5 mm was chosen that included shear bands or evidence of strain localisation identified with an optical microscope (Figure 10A). Each volume consisted of 4 scans stitched together using a field of view of 3.5 x 3.5 x 3.5 mm and a voxel size of 3.5 μm. Visualisation and filtering of the images were performed using Fiji and python scripts (Figure 10B) (Schindelin et al., 2012).

Semantic segmentation was carried out with the Ilastik interactive machine learning software using the pixel classification workflow (Berg et al., 2019). Feature selection and training was performed on 10 equally spaced images selected from the cropped and filtered image stack. In each image three different classes were identified corresponding to the coal, sandstone and background (Figure 10C). The segmentation workflow was then applied to the entire image stack. In a final step the output segmented image sequence was converted to a binary format in which the sandstone and background phase are white and the coal phase is black (Figure 10D).

A representative 250 x 250 x 250 pixel volume was selected from the segmented image which did not contain any decompression fractures. The binary image was then binned by a factor of 2 in all three dimension reducing the volume size to 125 x 125 x 125 pixels. Heterogeneity in the coal distribution within the volume was then characterized using a two-point probability function. The non-centred two-point probability function $S_2(r)$, which defines the probability (***P***) that two arbitrary points (x and x+r) are separated by a distance r are located in the same phase (*P*),

$$S_2(r) = \boldsymbol{P}(x \in P, x + r \in P) \qquad \text{for } x, r \in \mathbb{R}^2 \qquad (9)$$

was computed in three principal directions x, y and z and then an average calculated. This was performed using a python script from the open source PorousMediaGAN reconstruction tool (Mosser et al., 2017).

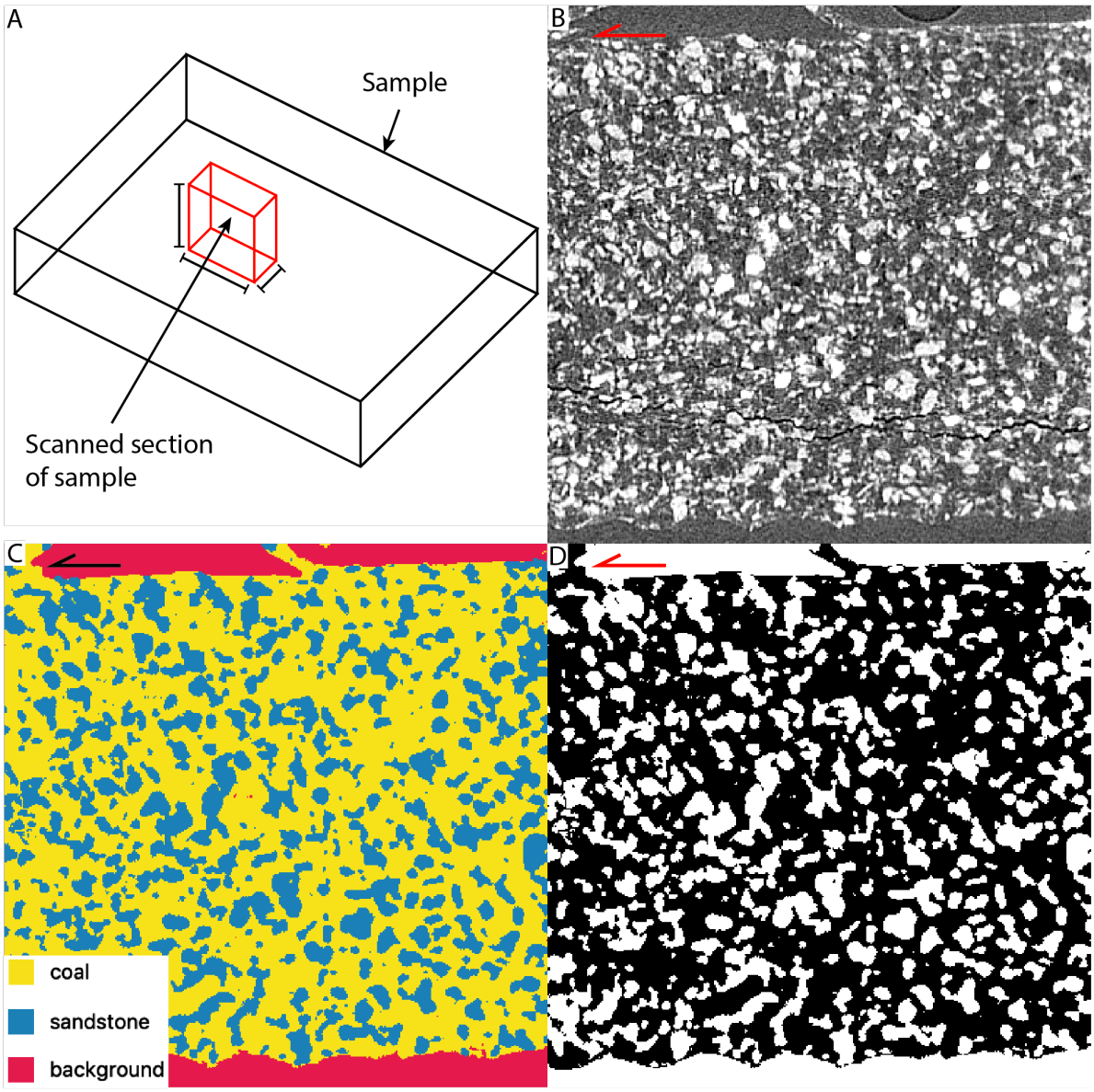

Figure 10: μCT scanning and segmentation procedure. (a) Diagram of approximate location of scan in sample. (b) Filtered μCT image slice of sample. NOTE: this is a cropped area of the larger images in order to illustrate the segmentation procedure. (c) Training image. (d) Segmented binary image slice. Black = coal phase.

2.3.2 SEM

A JEOL JCM-6000 table-top SEM and a Zeiss EVO 15 environmental SEM were used to study the microscale structure of the deformed fault gouge. Sections cut parallel with the shear direction were polished manually and with an Ion-beam polisher. Samples used in the table-top SEM were also coated with a ~5 nm thick layer of platinum to ensure adequate conduction with the sample.

2.3.3 Raman Spectroscopy

To characterise the development of coal maturity and changes in crystal structure upon shearing, Raman spectroscopy was performed using WiTec ALPHA300 R confocal Microscope. A laser wavelength of 532 nm and spectral grating of 600 g/mm was used in all scans and data acquisition, processing and peak fitting was performed using WiTec Project FIVE 5.2 and Fityk 1.3.1 curve fitting software (Wojdyr, 2010). Following the approach used by Sadezky et al. (2005) a combination of four Lorentz peaks (D1, D2, D4 and G) and one Gaussian peak (D3) were used to obtain a best fit of the data (Figure 6A). The degree of crystallinity of the coal was quantified using the intensity ratio $\left(\frac{ID}{IG}\right)$ and peak position of the D and G peaks. Note: in this report the D peak refers to the intensity and position of the D_1 peak (Figure 6A). In addition, the in-plane crystallite size (L_a) was quantified using equation 10 from Pimenta et al. (2007),

$$L_a = \frac{560}{E_{Laser}^4}\left(\frac{ID}{IG}\right)^{-1} \qquad (10)$$

in which E_{Laser} is the excitation laser energy in eV used in the analysis. Measurements of coal grains were taken at six locations in each sample, three points within the matrix and three points within the shear bands/ concentrated regions of coal. In addition, measurements at three randomly chosen points were taken from an unsheared sample composed of 100 wt% coal.

3 Results

3.1 Mechanical Data

Frictional data from all experiments performed on sandstone-coal fault gouge are presented in Figure 11A-D with key values outlined in table 1. All experiments were performed at a confining pressure of 55 MPa, pore fluid pressure of 15 MPa using DI water as the pore fluid and temperature of 100°C. The velocity step sequence used in the velocity stepping experiments was 0.1-1-10-1-10-1-10 μms^{-1} and the constant velocity experiments were performed at 1 μms^{-1}.

3.1.1 Frictional strength – Velocity stepping experiments

Velocity stepping experiments performed using gouges of 100 wt% Coal Cliff sandstone (s021) and 100 wt% Illawarra coal (s027) show a rapid near-linear increase in strength reaching similar peak friction coefficient (μ_{peak}) of 0.425 and 0.419 respectively within the first ~0.5 mm of displacement (Figure 11A). Post peak friction, s021 displays minor weakening before reaching a steady state friction coefficient of 0.387 after 1.3 mm of displacement. Then from 2.9 mm until the end of shearing (D_{tot} = 5.897 mm) a near linear displacement weakening trend is superimposed on the velocity steps. However, s027 (100 wt% coal) displays dramatic post peak displacement weakening before reaching steady state of 0.245 after ~2.5 mm of displacement. S023 (50 wt% coal) and s026 (75 wt% coal) display a similar μ_{peak} as the coal end member (s027) of 0.409 and 0.458 respectively. They both also display a similar post peak weakening trend within the first ~2.2 mm of displacement as s027 reaching a steady state of 0.224 and 0.231 respectively (Figure 11B). Experiment s027 remains at steady state until the end of shearing however s023 and s026 show minor near linear displacement weakening.

3.1.2 Frictional strength – Constant velocity experiments

The experiments performed at a constant slip velocity with 50 wt% coal (s041 and s031) have a similar μ_{peak} of 0.434 and 0.451 and show the same post peak displacement weakening trend observed in the velocity stepping experiments within the first ~2 mm of displacement (Figure 11C). s031 then exhibits linear displacement weakening until the end of shearing (D_{tot} = 5.161 mm). s040 (25 wt% coal, D_{tot} = 4.919 mm) displays a μ_{peak} of 0.452 and then post peak displacement weakening before reaching a μ_{ss} of 0.395 after 1.4 mm of displacement. This is followed by linear displacement hardening up to ~3 mm then displacement weakening until the end of shearing. S042 (25 wt% coal, D_{tot} = 1.5 mm) has a lower μ_{peak} of 0.428 but experiences only very minor post peak weakening until the end of shearing.

A constant velocity experiment was also performed on Slochteren sandstone gouge with 25 wt% coal (s033). This sample displays the same rapid near-linear increase in strength within the first ~0.5 mm of displacement although the peak strength of 0.573 is not reached until ~0.9 mm of shear displacement compared to 0.452 and 0.45 mm for the experiments with 100 wt% Coal Cliff sandstone and 25 wt% coal (Figure 11D). Furthermore, the post peak weakening within the first ~2 mm of displacement observed in experiments using Coal Cliff sandstone and coal was not observed. Then from 2.3 mm until the end of shearing (D_{tot} = 5.612 mm)

s033 displays near linear displacement weakening. Hunfield et al. (2017) performed a friction experiment on the Slochteren sandstone end member using the same experimental conditions used in this study which is plotted in Figure 11D. They obtained a μ_{peak} of 0.616 after ~2.4 mm of displacement and then observed minor linear weakening from ~3 mm until the end of shearing (D_{tot} = 5.49 mm).

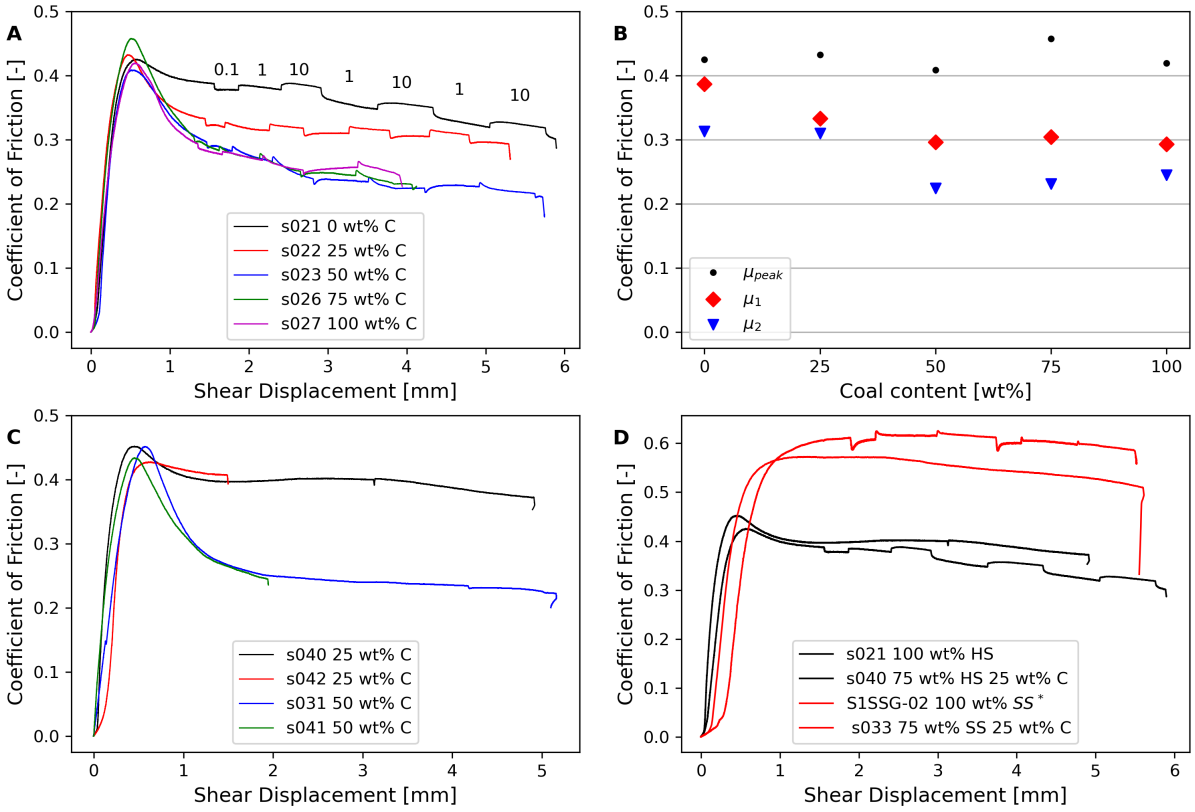

Figure 11: Frictional strength data from experiments performed on simulated sandstone-coal fault gouge in this study. See table 1 for full details of experimental conditions. * Friction data from Hunfield et al. (2017). (a) Coefficient of friction vs shear displacement of velocity stepping experiments. (b) Scatter plot of coefficient of friction vs coal content of velocity stepping experiments. μ_1 = friction coefficient at the time of the first velocity step, μ_{ss} = steady state friction coefficient or the value at $_{Dtot}$ if steady state is not reached. (c) Coefficient of friction vs shear displacement of constant velocity experiments. (d) Coefficient of friction vs shear displacement of Coal Cliff sandstone – Illawarra coal gouge and Slochteren sandstone – Illawarra coal fault gouge.

3.1.3 Velocity dependence of friction

The rate sensitivity parameter *(a-b)* and individual RSF parameters *a, b1, b2, d_{c1}* and *d_{c2}* were derived for four velocity steps; 0.1–1, 1-10, 10-1 and 1-10 μms^{-1} and are plotted against coal content in Figure 12 and detailed in Table 3. The two evolution parameters (*b1* and *b2*) were added together then subtracted from *a*, to obtain the rate sensitivity parameter.

The Coal Cliff sandstone end member shows velocity strengthening behaviour in all four velocity steps with *(a-b)* values between 0.0036 – 0.0075 (Figure 12D). The sample with 25 wt% coal is initially velocity weakening in the first two velocity steps however displays positive

(a-b) values in the third and fourth velocity steps. S023 (50 wt% coal) is velocity weakening in all velocity steps, initially only slightly with an *(a-b)* of -0.00045 before -0.0034 in the second velocity step. The weaking is considerably less in the down step (-0.00054) but then becomes more negative in the fourth velocity step (-0.0045). A similar trend is observed in the sample containing 75 wt% coal which also shows negative velocity dependence in all velocity steps with *(a-b)* values of -0.0062 and -0.0048 in the second and fourth steps, respectively. However, the Illawarra coal end member is velocity strengthening in the first velocity step then velocity weakening in the second before strengthening again in the final two steps. This trend implies that the presence of coal in sandstone-coal mixed fault gouges induces velocity weakening and that it causes stronger velocity weakening in samples containing ≥50 wt% coal.

The direct effect parameter, *a*, in the first velocity step (0.1–1 μms^{-1}) of the Coal Cliff sandstone end member is noticeably less (0.0030) than for both upsteps and downsteps between 1 and 10 μms^{-1} for which values range from 0.0030 to 0.0036 (Figure 12A). This same trend is emphasised in the sample containing 25 wt% coal which has value of 0.0034 for the first velocity step compared to 0.0047 to 0.0049 for velocity steps between 1 and 10 μms^{-1}. It is also observed in the Illawarra coal end member, the *a* value for the first step is considerably smaller than for the samples containing sandstone with a value of 0.0021. The direct effect in samples s023 (50 wt% coal) and s026 (75 wt% coal) increases from the first to the third velocity steps reaching peak values in the third step of 0.0047 and 0.0048 respectively and then decreases in the final step.

The first evolution parameter, *b1* in the clay rich Coal Cliff sandstone end member is negative in the 1-10 μms^{-1} upsteps (-0.0025) although only slightly negative in the 0.1-1 μms^{-1} up step and 10-1 μms^{-1} down step (Figure 12B). However, is positive in all velocity steps in the sample containing 25 wt% coal (s022) with values between 0.0006 and 0.00125. In sample s023 (50 wt% coal) and s026 (75 wt% coal) *b1* range from 0.00073 to 0.0048 and from 0.0018 to 0.004 respectively. The coal end member has a negative *b1* parameter in the first velocity step (-0.005) and ~0.0025 in the other velocity steps. The second evolution parameter *b2* in the Coal Cliff sandstone end member (s021) is close to 0 or slightly negative in all of the up steps but -0.002 in the down step (Figure 12C). The samples with 50 wt% and 75 wt% coal display similar *b2* values in the 0.1-1 μms^{-1} up step and 10-1 μms^{-1} down step of ~0.001 - 0.002. This trend is observed in the 1-10 μms^{-1} upsteps however *b2* values are ~0.004 – 0.0075. For the coal end member *b2* is ~0.002 in the first three velocity steps however in the final step from 1-10 μms^{-1} it is negative (-0.0022). The critical slip distance d_{c1} is between 0.3 and 0.9 mm in the velocity upsteps across all of the samples although is ~1.1 mm in the 10-1 μms^{-1} down step (Figure 12E). There is little variation in the second critical slip distance, d_{c2} within each sample however they decrease with increasing coal content (Figure 12F)

Table 3: Rate and state friction parameters.

Experiment	Velocity step [μms^{-1}]	*a*	*b1*	d_{c1} *[m]*	*b2*	d_{c2} *[m]*	*a-b*
S021	0.1 -> 1	0.00301	-0.00076	0.00003	0.00020	0.00020	0.00356
(0 wt% Coal)	1 -> 10	0.00360	-0.00285	0.00005	-0.00029	0.00026	0.00674
	10 -> 1	0.00421	-0.00010	0.00007	-0.00205	0.00026	0.00636
	1 -> 10	0.00341	-0.00235	0.00006	-0.00005	0.00040	0.00581
s022	0.1 -> 1	0.00343	0.00125	0.00006	0.00451	0.00014	-0.00233
(25 wt% Coal)	1 -> 10	0.00472	0.00088	0.00001	0.00435	0.00027	-0.00051
	10 -> 1	0.00585	0.00060	0.00030	0.00185	0.00010	0.00340
	1 -> 10	0.00489	0.00063	0.00002	0.00295	0.00021	0.00130
s023	0.1 -> 1	0.00360	0.00200	0.00003	0.00205	0.00008	-0.00045
(50 wt% Coal)	1 -> 10	0.00399	0.00073	0.00002	0.00668	0.00007	-0.00342
	10 -> 1	0.00476	0.00480	0.00009	0.00050	0.00010	-0.00054
	1 -> 10	0.00330	0.00380	0.00004	0.00400	0.00010	-0.00450
s026	0.1 -> 1	0.00292	0.00178	0.00003	0.00209	0.00006	-0.00095
(75 wt% Coal)	1 -> 10	0.00428	0.00300	0.00003	0.00750	0.00020	-0.00621
	10 -> 1	0.00485	0.00400	0.00010	0.00100	0.00017	-0.00015
	1 -> 10	0.00366	0.00181	0.00003	0.00665	0.00014	-0.00479
s027	0.1 -> 1	0.00211	-0.00050	0.00004	0.00120	0.00009	0.00141
(100 wt% Coal)	1 -> 10	0.00387	0.00301	0.00002	0.00231	0.00006	-0.00145
	10 -> 1	0.00380	0.00185	0.00016	0.00150	0.00003	0.00045
	1 -> 10	0.00425	0.00264	0.00002	-0.00215	0.00009	0.00375

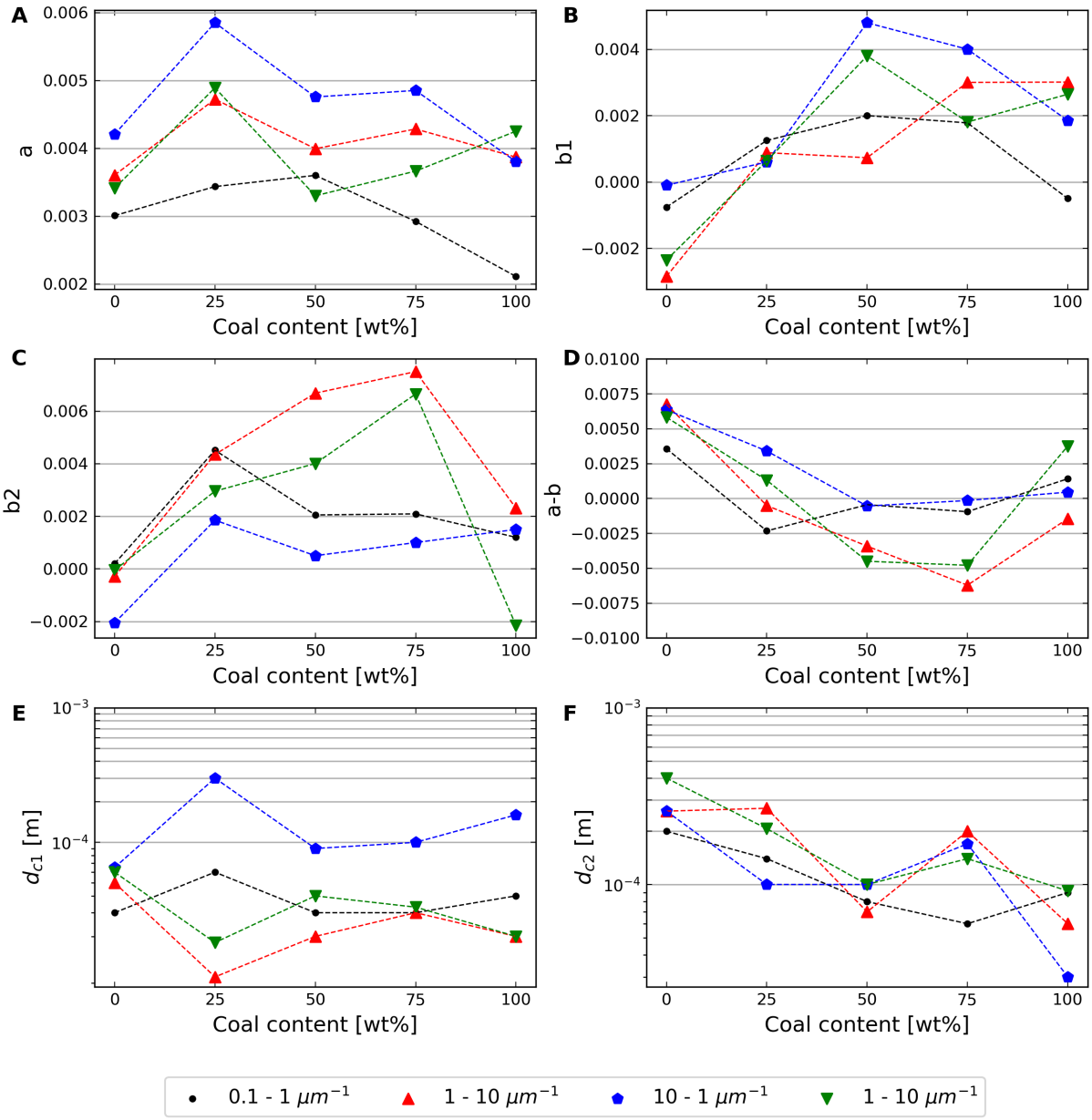

Figure 12: Rate-and-state friction parameters vs coal content for four velocity steps. Velocity stepping sequence: 1->0.1->1->10->1->10->1->10 μms^{-1}. (a) *a*. (b) *b2*. (c) *b2*. (d) *(a-b)*. (e) d_{c1}. (f) d_{c2}.

3.2 Microstructure

As mentioned in section 2.3, microstructural analysis was performed on four samples from experiments at constant velocity using mixed sandstone-coal fault gouges, s042 (25 wt% coal, D_{tot} = 1.5 mm) & s040 (25 wt% coal, D_{tot} = 4.919 mm) and s041 (50 wt% coal, D_{tot} = 1.948 mm) & s031 (50 wt% coal, D_{tot} = 5.161 mm) using a combination of XCT, quantitative image analysis and SEM. XCT and quantitative image analysis was also performed on two additional samples with 25 wt% (Pre25) and 50 wt% (Pre50) coal prepared following the procedure set out in section 2.2.1 however were not deformed in the apparatus. This provided information about the microstructure of the gouge prior to shearing. Samples were preserved in Epoxy resin and then cut parallel with the shear direction. The classification scheme outlined in Logan et al. (1992) was used to describe the features and textures observed in the microstructure of

the samples, see section 1.2.1 and Figure 2 for theoretical background. It should be noted that complete sample recovery was not achieved in all samples and structures may have been distorted or damaged by preserving them in Epoxy resin.

3.2.1 X-ray microscopy

Sample s042 (25 wt% coal, D_{tot} = 1.5 mm) displays discontinuous R_1 shears which extend partially across the thickness of the gouge (Figure 13A). In addition, a Boundary shear is present along the top of the sample composed of intensely comminuted quartz grains. However, it is not continuous implying that it has only accommodated a limited amount of displacement. Furthermore, the imprint of the grooves from the porous plates is visible along the lower and upper surfaces of the gouge indicating good sample recovery. Sample s040 (25 wt% coal, D_{tot} = 4.919 mm), which was sheared to a longer displacement displays a continuous R_1 shear which propagates through the gouge as well as discontinuous R_2 shears (Figure 13C). An ultra-fine grained B shear ~50 μm thick composed of quartz is observed along the top boundary of the sample. Poor sample recovery meant the complete structure was not retained however the smooth top boundary implies that a continuous Boundary shear did develop. The matrix in both s040 and s042 is composed of angular coal and quartz grains with sparse pyrite grains although there is no evidence of the development of a foliation (Figure 13).

The microstructure of sample s041 (50 wt% coal, D_{tot} = 1.948 mm) is characterized by coal rich zones which contain sparse quartz grains (Figure 14A). These oval shaped zones have a similar inclination (~10°) to R_1 shears in s031 (50 wt% coal, D_{tot} = 5.161 mm) suggesting that they may be associated with strain localisation. Numerous dilatant fractures are also present along what were likely to be incipient R_1 shears. There is limited evidence of grain size reduction along the boundary of the sample, however there is additional evidence of localisation in the form of R_2 shears (Figure 14B). The clay grains observed between coal grains, seen in the samples with 25 wt% coal, are also present in this sample. A continuous ultra-fine grained B shear, ~50 μm thick is present in sample s031 which contains some larger quartz grains. There is also a continuous R_1 shear which extends across the thickness of the gouge, however the sample has split along the riedel shear which likely occurred during decompression. The oval shaped zones seen in s041 (50 wt% coal, D_{tot} = 1.948 mm) are also present within the matrix of s031 however they are far less numerous.
The unsheared samples with 25 wt% (Pre25) and 50 wt% (Pre50) coal showed a homogeneous structure. Crucially the oval shaped coal rich zones seen in s041 (50 wt% coal) and s031 (50 wt% coal) are not observed in the unsheared sample.

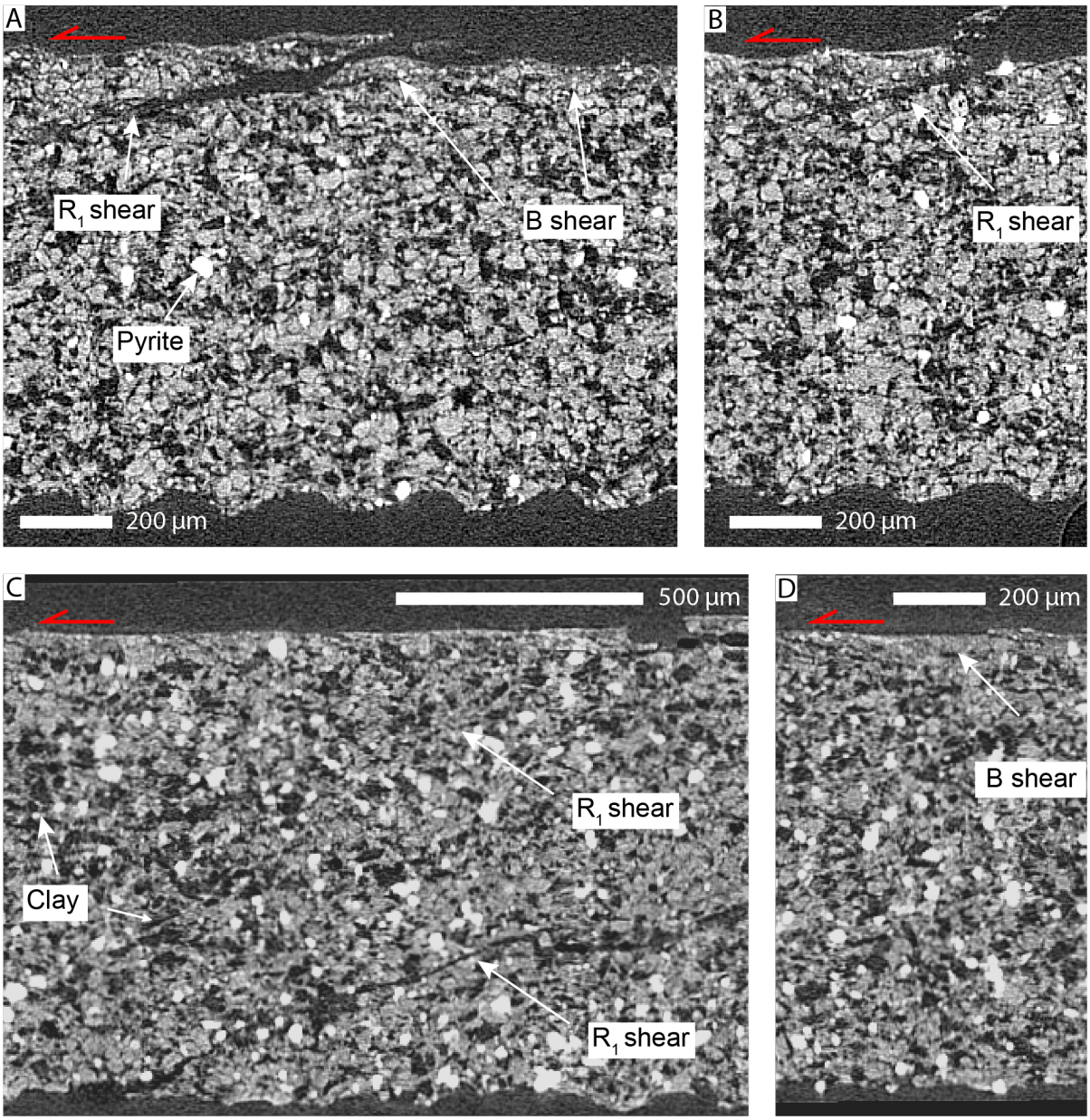

Figure 13: X-ray microscope images of sandstone–coal samples containing 25 wt% coal. Shear sense of in images is top to the left. (a & b) Sample s042 (D_{tot}= 1.5 mm) displays discontinuous R_1 shears plus grain size reduction along the B shear at the top surface of the sample. Pyrite grains are also observed (bright white grains). Note a & b are taken from different positions within the sample. (c & d) Sample s040 (D_{tot}= 4.919 mm). Continuous R_1 shears and fine-grained B shear. Coal is distributed within the matrix of both s040 and s042 with no evidence of accumulation of coal where strain localises (R_1 or B shears).

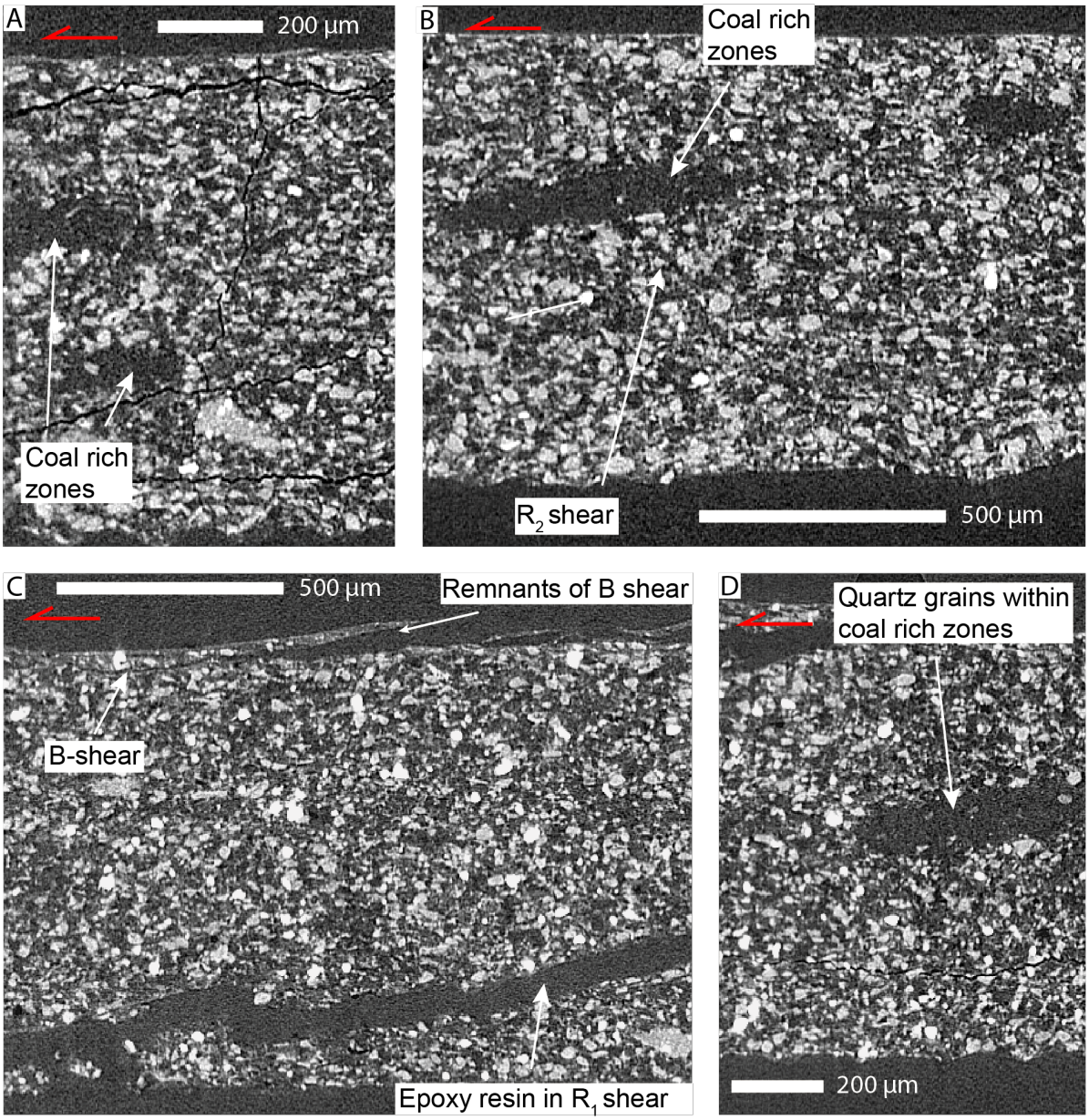

Figure 14: X-ray microscope images of sandstone-coal samples containing 50 wt% coal. (a & b) Sample s041 (D_{tot}= 1.948 mm). R_2 shears and numerous dilatant fractures which have an R_1 shear orientation. Coal rich zones are not laterally continuous through the gouge layer. (c & d) Sample s031 (D_{tot} = 5.161 mm). Fractures in the Y-shear orientation imply localisation.

3.2.2 Quantitative image analysis

As previously stated, a two-point correlation function was used to quantify the heterogeneity in the coal distribution within the matrix of the samples. XCT images were segmented and then converted to a binary format, from which a 250 x 250 x 250 pixel volume was chosen which did not contain any decompression fractures as this would skew the data. The pixel size in the XCT image is 3.5 µm. The binary image was then binned to reduce the size of the image to 125 x 125 x 125 pixels. The two-point correlation was then performed on the black phase in the binary image which represents the coal. Refer to section 2.3.1 for detail. The original XCT images and results of the correlation on the samples containing 25 wt% coal (Pre25,

s042 and s040) and 50 wt% coal (Pre50, s041, s031) are shown in Figure 15 and 16 respectively. The average scaled autocovariance is also presented in Figure 17.

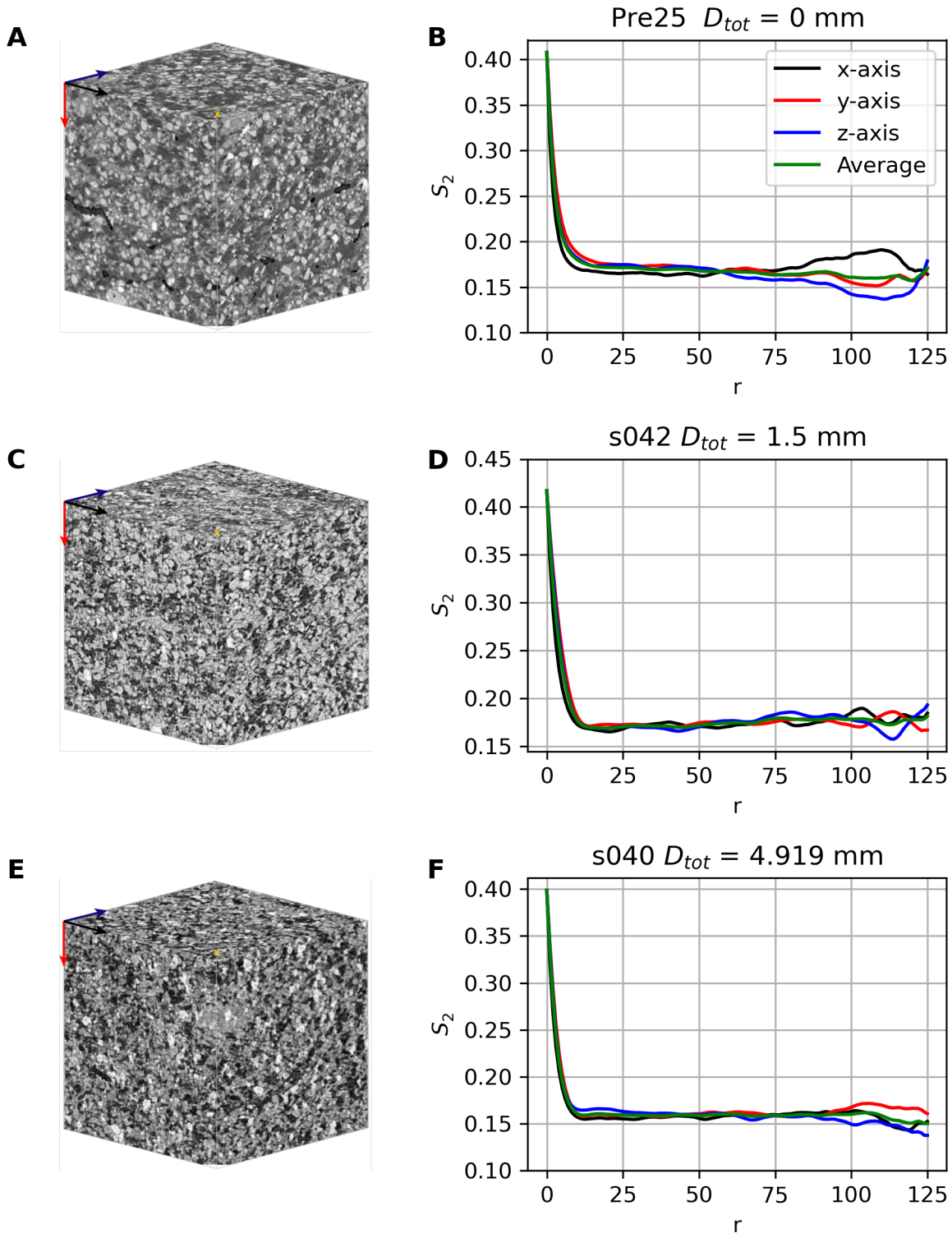

Figure 15: Two-point probability function calculated of the coal phase along principal axis of samples with 25 wt% coal. X axis is parallel with the shear direction. (a) XCT image of Pre25. (b) S_2 of Pre25. (c) XCT image of s042. (d) S_2 of s042. (e) XCT image of s040. (f) S_2 of s040.

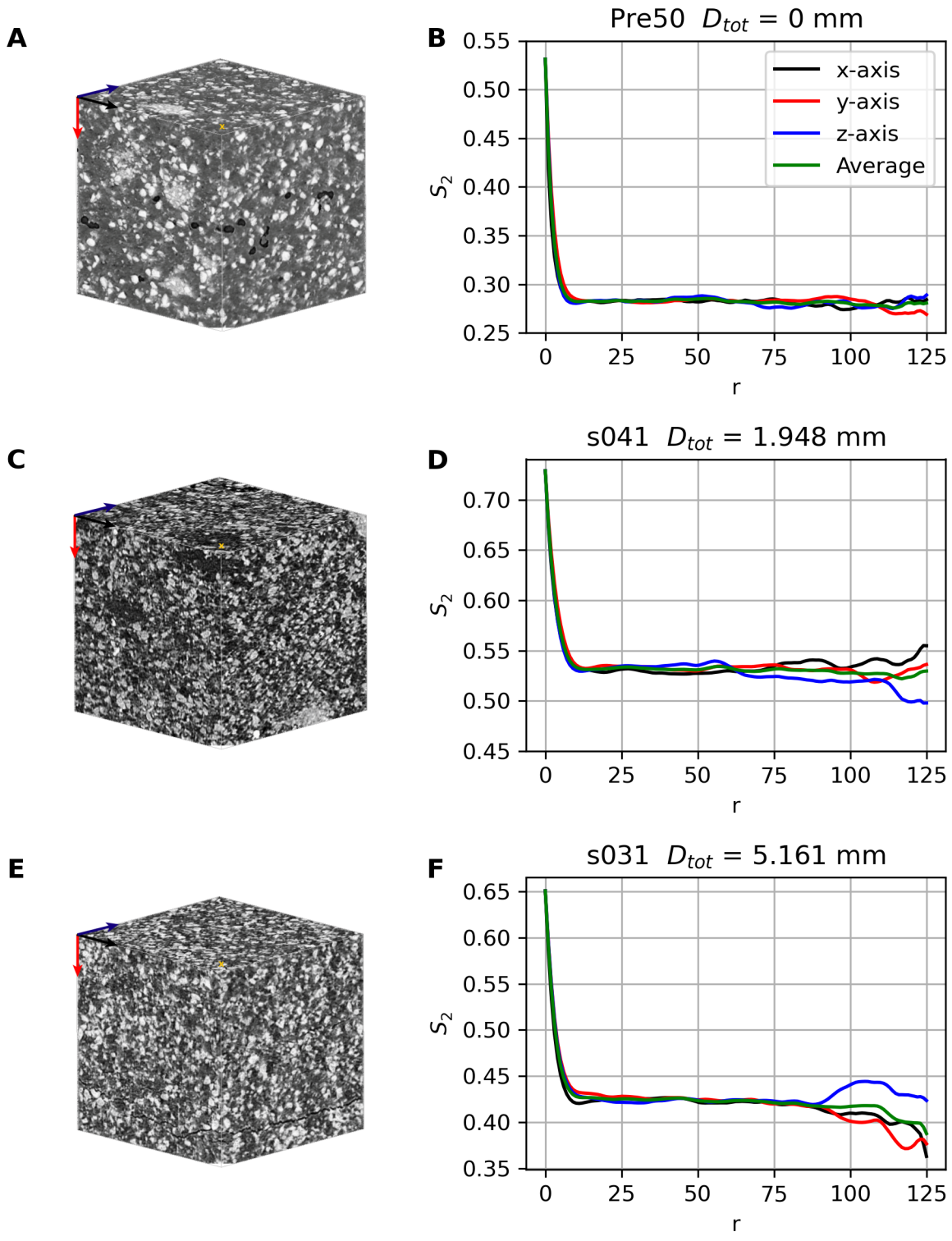

Figure 16: Two-point probability function calculated for the coal phase along principal axis of samples with 50 wt% coal. X-axis is parallel with the shear direction. (a) XCT image of Pre50. (b) S_2 of Pre50. (c) XCT image of s042. (d) S_2 of s042. (e) XCT image of s031. (d) S_2 of s031.

The distribution of coal within s042 (25 wt% coal, D_{tot} = 1.5 mm) and s040 (25 wt% coal, D_{tot} = 4.919 mm) is almost entirely homogeneous along all three axes (Figure 15D & F). In sample Pre25 (D_{tot} = 0 mm) the higher probability at larger r values along the x axis is likely to be due

to insufficient mixing of the gouge during sample preparation (Figure 15B). Coal distribution in the pre sheared sample containing 50 wt% coal (Pre50) is almost perfectly homogeneous (Figure 16B). The distribution becomes slightly heterogenous in s041 (50 wt% coal, D_{tot} = 1.948 mm) which may be representative of the coal rich patches seen in the original XCT image (Figure 16C). In sample s031 (50 wt% coal, D_{tot} = 5.161 mm) the distribution is entirely homogenous along all three axes when r is between ~10 and ~85 px. Between ~85 and 125 px there is apparent lateral ordering in the sample however it decreases along the x and y axis.

In samples Pre25, s042 and s040, all of which contain 25 wt% coal, S_2 = ~0.4 when r = 0. This implies 40% of the segmented volume is coal while the starting sample contained 25 wt% coal (Figure 15). Similarly at r = 0 in Pre50, s041 and s031 (all contain 50 wt% coal) S_2 is 0.53, 0.73 and 0.65 respectively (Figure 16). To enable comparison to be drawn between the samples, the average scaled autocovariance ($S_2^{(2)}$) was calculated which is plotted in Figure 17. Evidently variations in probability identified in Figure 15 and 16 are only minor.

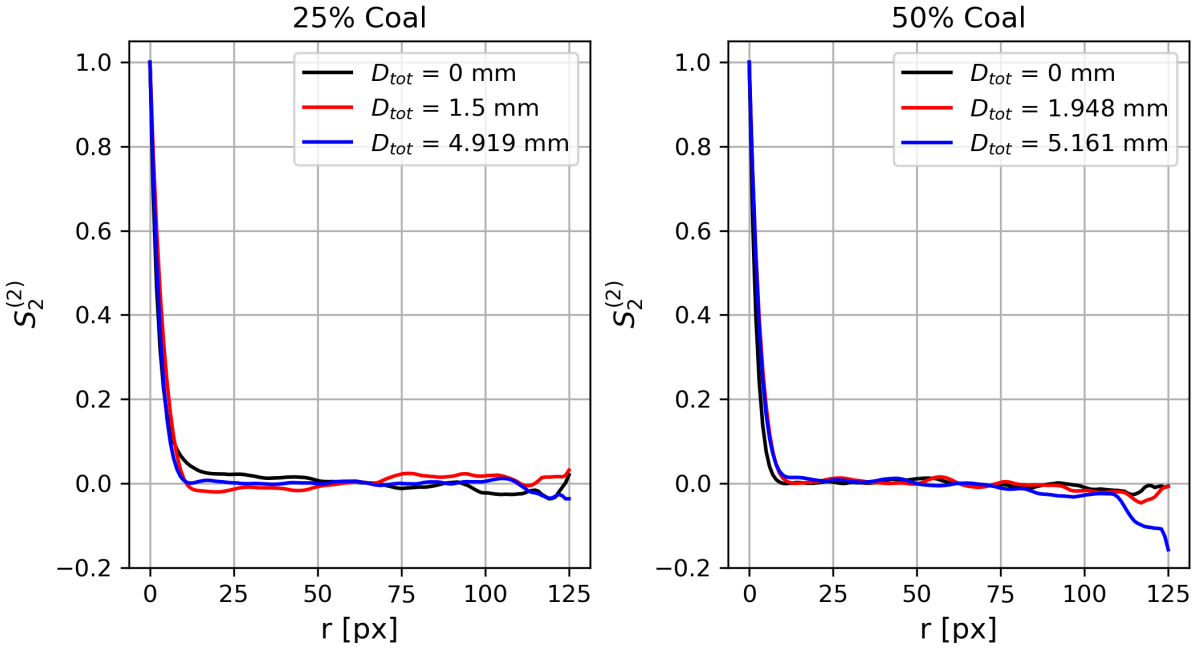

Figure 17: Average scaled autocovariance of coal phase. (a) 25 wt% coal. (b) 50 wt% coal.

3.2.3 SEM

Both samples containing 25 wt% coal (s040 & s042) display a fine-grained B-shear ~50 μm thick, composed of predominantly rounded to sub rounded quartz grains (d = 1 – 5 μm) (Figure 18B). Intergranular clay grains (d = 250nm - 1 μm) are visible in the B-shear in s042 (D_{tot} = 1.5 mm), however there is no foliation. Much of the B-shear in s040 (D_{tot} = 4.919 mm) was not recovered so it is not possible to determine the degree of continuity. The matrix in both samples is chaotic and composed of angular to sub angular quartz and coal grains (~10 – 40 μm) which are also truncated by R_1 shears in locations.

The B-shear in s041 (50 wt% coal, D_{tot} = 1.948 mm) is composed of sub rounded – sub angular quartz grains (d = 2 – 20 μm) and ellipsoidal coal grains (d = ~10 μm) (Figure 18A). These grains are surrounded by finer grained material (d <1 μm) composed of a combination of

Quartz, clay and coal. In comparison, the B-shear of sample s031 (50 wt% coal, D_{tot} = 5.161 mm) is composed of rounded to sub rounded coal grains (d = 500 nm - 3 μm) surrounded by aligned clay minerals, identified using EDX as kaolinite (Figure 19B). The clay minerals define a foliation that is close to anastomosing in parts of the B-shear (Figure 18C). Larger sub angular quartz grains (d = 2 – 20 μm) are also present, many of which contain intragranular fractures. The matrix is composed of larger angular to sub rounded quartz and coal grains (d = 10 – 40 μm) with regions of intense grain size reduction along R_1 shears (d < 1 μm). However, there is no foliation in the matrix which also has a chaotic microstructure. In addition, Illite is also present in microfractures within individual coal grains (Figure 19A).

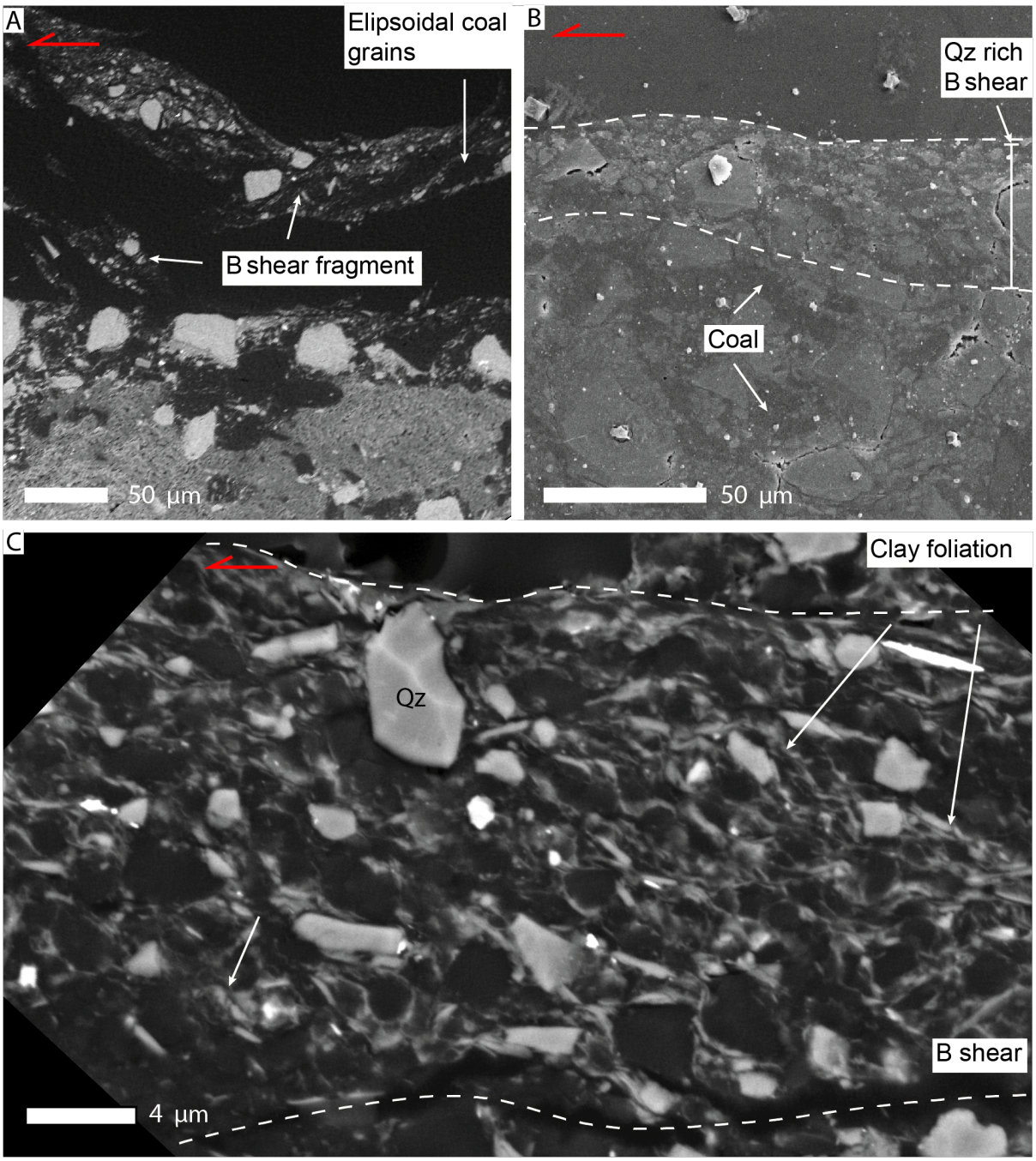

Figure 18: SEM images of boundary shear. (a) BSE-SEM image of sample s041(50 wt% coal, D_{tot} = 1.948 mm), discontinuous B-shear detached from sample. B-shear contains ellipsoidal coal grains within a close to anatomising foliation composed of clay grains. Evidence of grains size reduction of coal and quartz material. Matrix composed of large quartz and coal grains. (b) SEI-SEM image of Sample s042 (25 wt% coal, D_{tot} = 1.5 mm), continuous nanogranular quartz rich B-shear. (c) BSE-SEM image of sample s031 (50 wt% coal, D_{tot} = 5.161 mm). Clay foliation is close to anastomosing in certain regions. Foliation surrounds rounded to sub rounded coal grains.

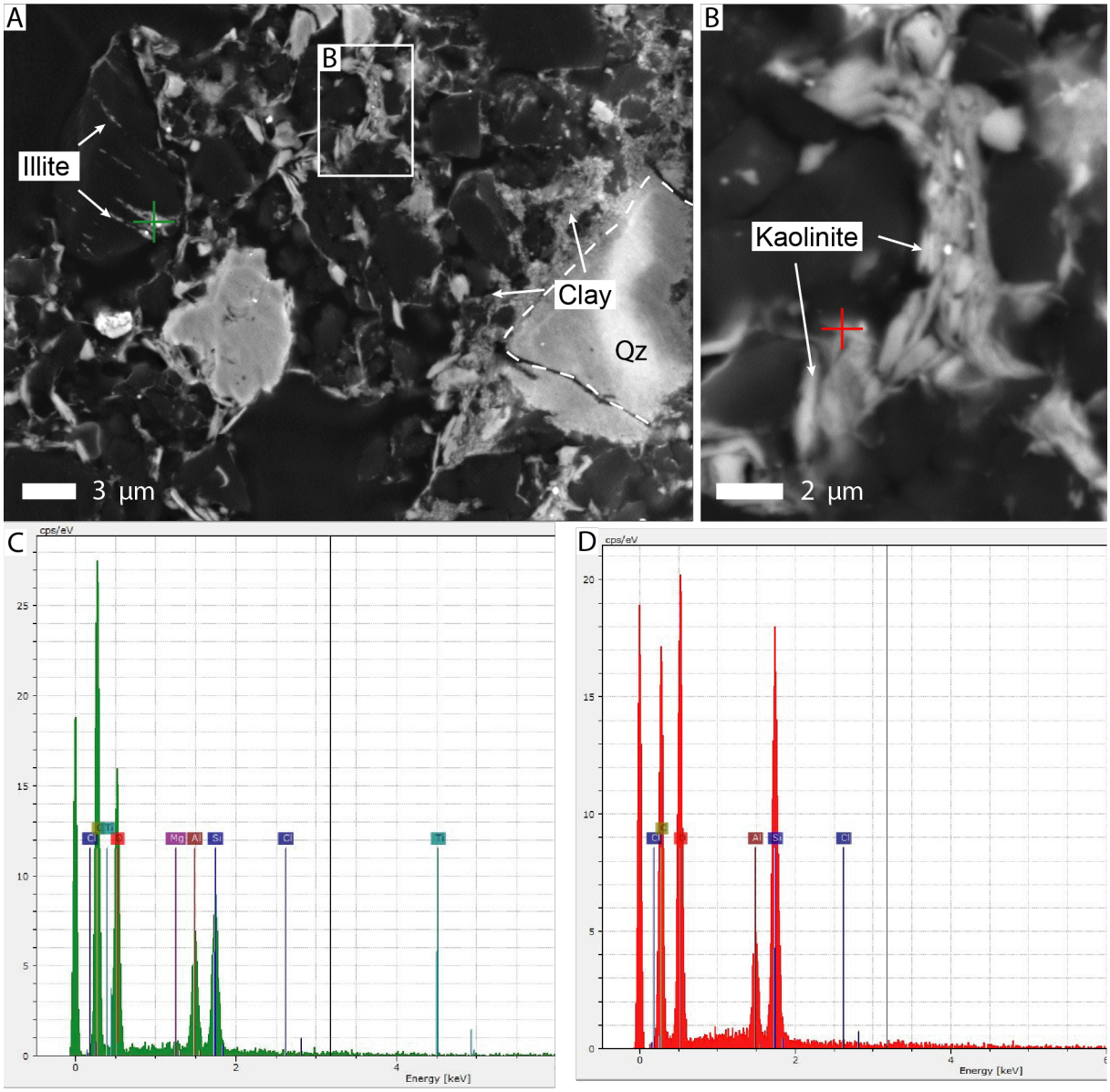

Figure 19: BSE-SEM images of clay minerals. Both images of sample s031 (50 wt% coal, D_{tot} = 5.161 mm). (a) Illite within intragranular cracks in coal grains. Clay minerals surrounding large angular quartz grains. (b) Intergranular kaolinite. (c) EDX spectra. Location of measurement indicated by green cross in Fig. 18A. (d) EDX spectra. Location of measurement indicated by red cross in Fig. 18B.

3.3 Raman spectroscopy

The peak position and intensity ratio between the D and G peaks in the Raman spectrum of Carbon was used to study the evolution of the crystallinity of coal under shearing. Raman parameters derived from the spectra are shown in Figure 20 and table 4. See Appendix 2 for the fitted spectra used in the study.

The $\left(\frac{I_D}{I_G}\right)$ value of the coal end member pre shearing is 0.768 ± 0.035 indicating that the coal is already crystalline pre shearing (Figure 20A). There is a noticeable decrease in $\left(\frac{I_D}{I_G}\right)$ in s041 (50 wt% coal, D_{tot} = 1.948 mm) however there is almost no difference between the B-shear (0.737 ± 0.037) and matrix (0.742 ± 0.0315). In comparison s042 (25 wt% coal, D_{tot} = 1.5 mm) shows no change in intensity ratio which still falls within one standard deviation of the pre sheared 100 wt% coal sample (s0XX). This is also the case for the matrix in s040 (25 wt% coal, D_{tot} = 4.919 mm) although there is a slight increase in the intensity ratio of the coal in the B-shear. In comparison $\left(\frac{I_D}{I_G}\right)$ of the B-shear (0.6819 ± 0.0034) and the matrix (0.7187 ± 0.0383) in s031 (50 wt% coal, D_{tot} = 5.161 mm) is smaller than s041. Therefore $\left(\frac{I_D}{I_G}\right)$ in coal rich samples decreases with displacement indicating a change in the molecular structure of the coal. The position of D peak shows no discernible trend with either coal content or shear displacement (Figure 20C). However, the position of the G peak does shift to higher frequencies with increasing displacement. Nonetheless in samples with 25 wt% coal (s042 and s040) the G peak position falls within one standard deviation of the G peak position in the pre sheard sample (1591.327 cm^{-1} ± 1.016). The G peak position in the B-shear and matrix in s041 (50 wt% coal, D_{tot} = 1.948 mm) shifts to 1593.039 cm^{-1} ± 9.86 and 1596.294 cm^{-1} ± 6.452 respectively. In addition, there is no difference in the G peak position between s041 and s031 (50 wt% coal) the latter of which was sheared to 5.161 mm of displacement. As the in-plane crystallite size (L_a) is related to the intensity ratio between the D and G peaks, L_a increases with shear displacement in the coal rich samples (Figure 20B). However, the samples with 25 wt% coal (s042 and s040) display only minor change which is within one standard deviation of the pre sheared 100% coal sample.

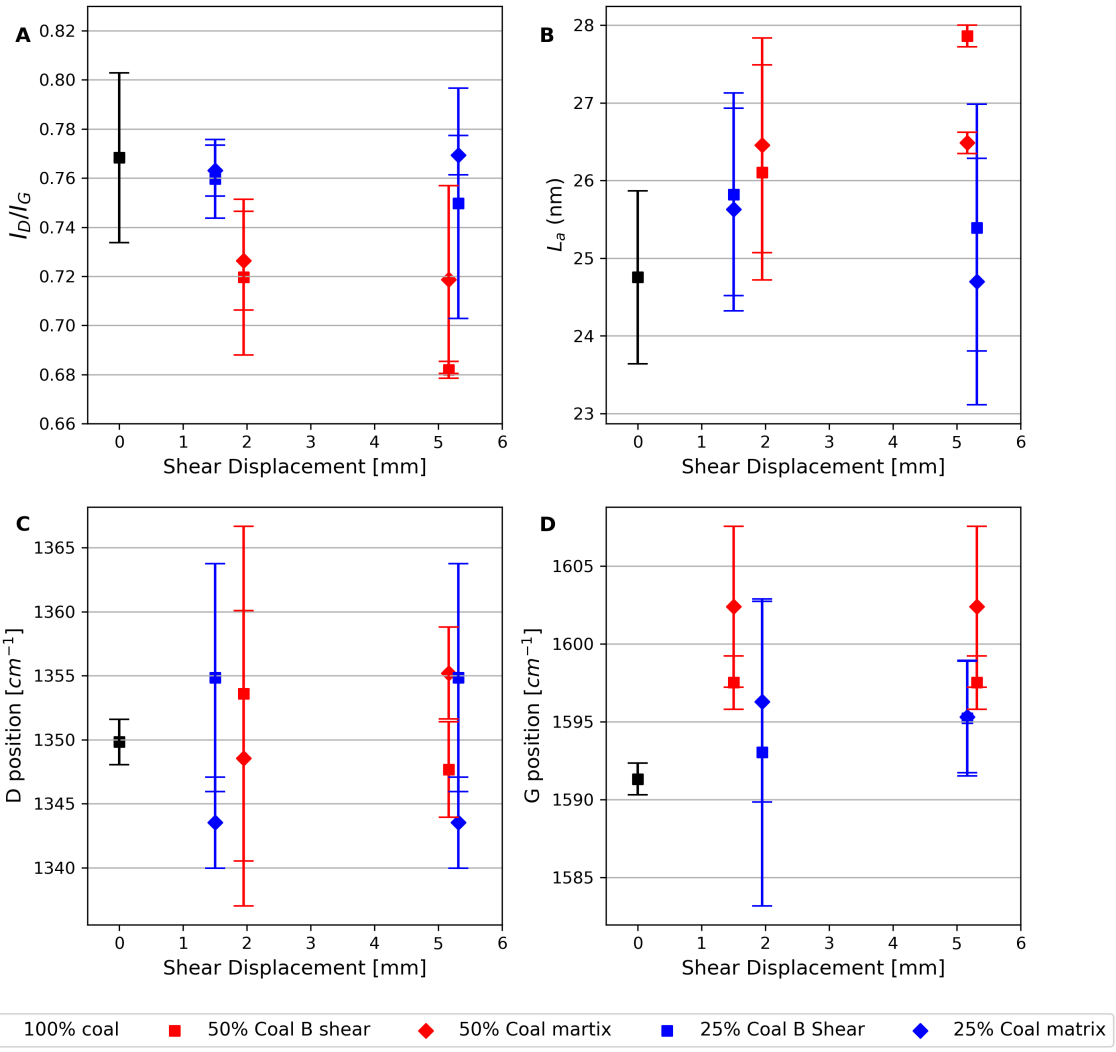

Figure 20: Raman parameters derived from best fit spectra. (a) Intensity ratio, $\left(\frac{I_D}{I_G}\right)$ between the D and G peaks. (b) In plane crystallite size L_a. (c) Position of D peak. (d) Position of G peak.

Table 4: Raman parameters.

Experiment	Raman parameter	Boundary shear	Boundary shear err	Matrix	Matrix err
s042	I_D/I_G	0.7497	0.0469	0.7693	0.0080
(25 wt% Coal)	D position [cm^{-1}]	1354.8567	8.8891	1343.5368	3.5607
D_{tot} = 1.5 mm	G position [cm^{-1}]	1597.5150	1.7243	1602.3900	5.1698
	L_a (nm)	25.3938	1.5876	24.6998	0.2575
s040	I_D/I_G	0.7597	0.0160	0.7631	0.0104
(25 wt% Coal)	D position [cm^{-1}]	1346.6795	9.5043	1352.7612	7.6819
D_{tot} = 4.919 mm	G position [cm^{-1}]	1593.2434	8.0606	1591.4161	2.4405
	L_a (nm)	25.0187	0.5317	24.9019	0.3407
s041	I_D/I_G	0.7197	0.0317	0.7264	0.0202
(50 wt% Coal)	D position [cm^{-1}]	1353.5948	13.0725	1348.5656	11.5281
D_{tot} = 1.948 mm	G position [cm^{-1}]	1593.0390	9.8595	1596.2940	6.4516
	L_a (nm)	25.8212	1.3045	25.6287	1.1165
s031	I_D/I_G	0.6819	0.0034	0.7187	0.0383
(50 wt% Coal)	D position [cm^{-1}]	1347.6838	1.4757	1355.2075	8.0995
D_{tot} = 5.161 mm	G position [cm^{-1}]	1595.2330	3.7216	1595.3144	3.5887
	L_a (nm)	27.8629	0.1384	26.4854	1.4017
s0XX	I_D/I_G	0.7683	0.0346		
(100 wt% Coal)	D position [cm^{-1}]	1349.8290	1.7789		
D_{tot} = 0 mm	G position [cm^{-1}]	1591.3274	1.0156		
	L_a (nm)	24.7552	1.1141		

4 Discussion

The objective of this study was to investigate the influence of coal on the frictional properties of the Coal Cliff sandstone. In doing so this will contribute to the assessment of the seismic hazard of faults in the Sydney basin. Friction experiments performed on Coal Cliff sandstone–coal simulated fault gouge, identified a number of key findings including:

1. The Coal Cliff sandstone is inherently weak, independently of coal.
2. Fault gouge samples which contain ≥50 wt% coal experience intense post peak displacement weakening.
3. Coal Cliff sandstone and Illawarra coal end members display velocity strengthening values at 1 and 10 μms^{-1} whereas coal rich (≥50 wt% coal) sandstone-coal samples exhibit velocity weakening at both velocities.
4. Samples with ≥ 50 wt% coal develop fine grained coal rich shear bands.

In the following I will integrate the mechanical data, microstructural observations, and Raman data to identify likely deformation mechanisms controlling fault friction. Comparisons will also be drawn with the findings of similar studies on weak phase material. In addition, I will discuss the implications of the results for the stability of faults in the Sydney basin and Groningen gas field.

4.1 Frictional strength

4.1.1 Coal Cliff Sandstone

XRD analysis indicated that the Coal Cliff sandstone used in these experiments contains a high clay content (44.1 wt%). Therefore, I will first consider the influence of clay on fault friction before addressing the influence of coal. The influence of phyllosilicate minerals, including both swelling (Takahashi et al., 2007; Tembe et al., 2010) and non-swelling clays (Crawford et al., 2008) on friction is widely reported and it has been demonstrated that clay rich (> 40 wt%) fault gouges are frictionally weak. In triaxial experiments on kaolinite-quartz gouge mixtures Crawford et al. (2008) observed a considerable reduction in grain comminution in samples containing >30wt% clay, due to the lubricating effect of clay. They reported the preservation of large relic (original) grains similar to those observed in the samples found in this study, as seen in Figure 19A. Furthermore, Haines et al. (2013) suggested that very thin clay layers within R_1, B and Y shears enable deformation to occur with only limited dilation due to grain sliding or cataclasis. Considering that the Slochteren Sandstone has a clay content of ~4% and μ_{peak} = 0.626 it is reasonable to conclude that the presence of a larger amount of clay is the cause of low friction in the samples containing 100 wt% and 75 wt% Coal Cliff sandstone. Furthermore, these samples have a μ_{peak} = 0.425 and 0.452 respectively which is comparable to that of the quartz-clay sample containing 40 wt% Kaolinite (μ_{peak} = ~0.45) from Crawford et al. (2008). However, the authors report strain hardening following peak strength whereas strain/displacement weakening and steady state sliding was observed in s021 (0 wt% coal) and s022 (25 wt% coal) respectively. The latter is likely due to the influence of the small component of coal (25 wt%).

4.1.2 Illawarra coal and mixed sandstone - coal gouge

The coal rich samples containing ≥50 wt% coal (s023, s026, s027, s031, s041) have a similar μ_{peak} = 0.409 – 0.458 and all display intense post peak displacement weakening reaching a μ_{ss} = 0.224 – 0.245, independent of coal content. As these samples display the same friction trend as the pure coal end member, this implies that coal is controlling friction in all of these samples. Furthermore, the microstructure of s041 (50 wt% coal, D_{tot} = 1.949 mm) and s042 (25 wt% coal, D_{tot} = 1.5 mm) is markedly different. S042 has discontinuous R_1 and B shears which is consistent with the predicated microstructure at that displacement following the Logan et al. (1979) classification (Figure 13A & B). In addition, the B shear is composed of fine-grained quartz surrounded by clay grains implying that comminution plays a role in strain localisation (Figure 18B).

s041 (50 wt% coal, D_{tot} = 1.949 mm) also displays R_1, R_2 and a discontinuous B shear (Figure 14A & B), however the B shear is enriched with fine grained coal grains (Figure 18A). This suggests that the enrichment of coal where strain localises may be related to the post peak weakening seen in the coal rich samples (≥50 wt% coal). The enrichment process likely operates through smearing of coal into shear bands however it is difficult to constrain over what displacement the smearing occurs. It is possible that 50 wt% represents a threshold coal content for smearing to occur. Nonetheless as the coal rich sandstone–coal samples follow the same weakening trend as the coal end member (s027), smearing would only play a role in the very early stages of post peak weakening. In addition, for smearing to occur a planar structure or surface must first develop and at this stage only incipient R_1 shears will have developed. s041 also contains peculiar oval shaped coal rich zones which are inclined at angles of ~10 – 15^o to the shear direction, similar to the orientation in which R_1 shears develop, implying they may be associated with strain localisation (Figure 14A & B). These features are not visible in the pre sheared sample containing 50 wt% coal. Furthermore, the quantitative image analysis indicates that the distribution of coal is close to homogeneous in the pre sheared sample (Pre50, 50 wt% coal, D_{tot} = 0 mm), demonstrating that the coal rich zones are not caused by poor mixing of the starting gouge (Figure 16B). Considering that the coal rich zones form within the first ~2 mm it is likely that they developed during compaction and then rotate and are elongated in the early stages of strain localisation as the stress field rotates. Only a few of these features are also present in s031 (50% coal, D_{tot} = 5.161 mm) indicating that they may be destroyed or mixed into the matrix at longer displacements. It is also worth highlighting Liu et al. (2020) do not report similar coal rich zones in their samples of Carboniferous shale-coal fault gouge. They did perform some shorter displacement experiments (D_{tot} < 2.5 mm) however the authors did not perform microstructural analysis on these samples.

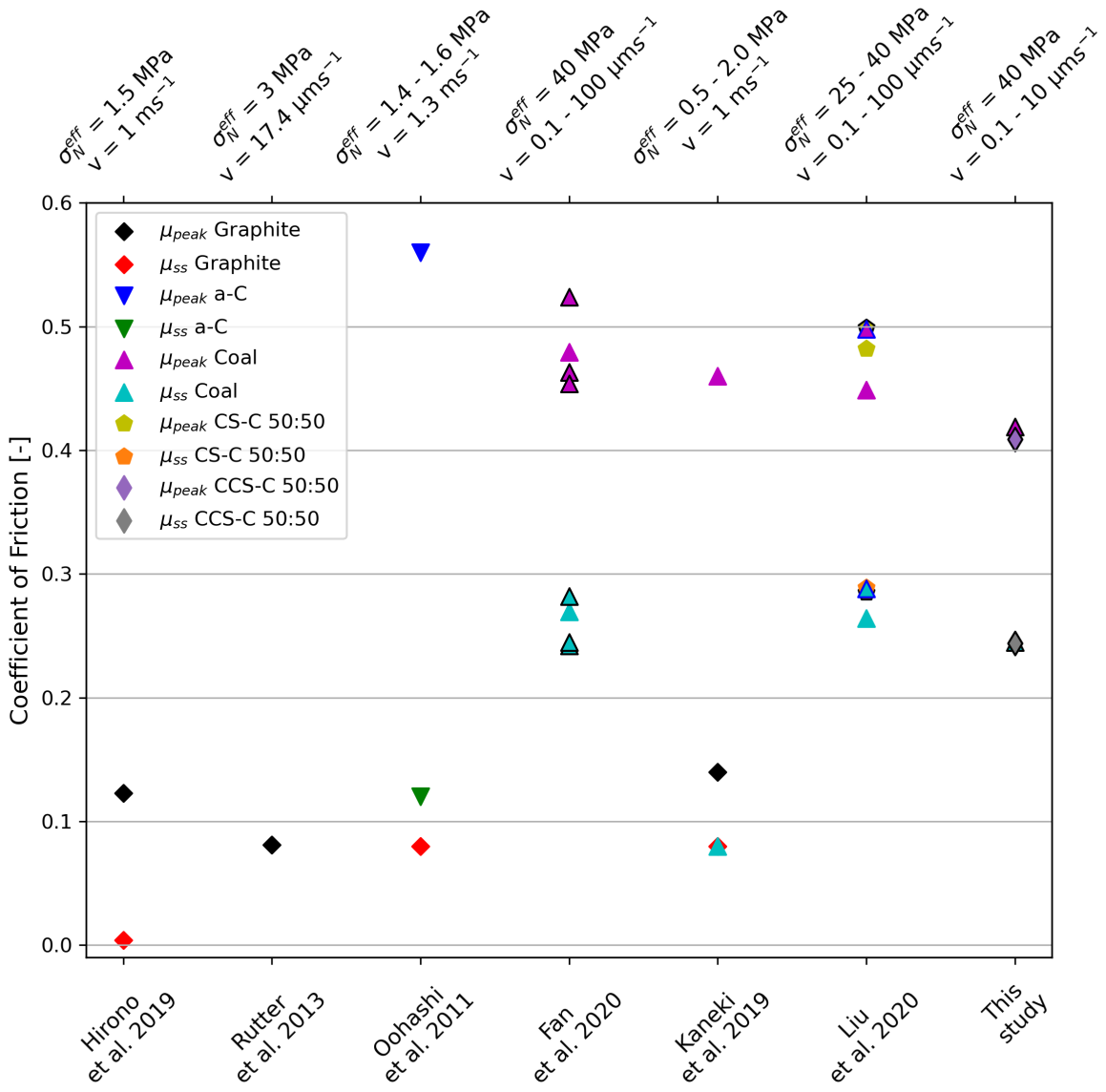

Figure 21: Plot of peak and steady state friction coefficient of recent studies on Carbonaceous materials. σ_N^{eff} = effective normal stress, v = slip velocity, a-C = amorphous Carbon, CS = Carboniferous shale, CCS = Coal Cliff sandstone. Black outline on marker indicates experiments performed at P_f = 15 MPa with H_2O. Blue outline on marker indicates experiments performed at P_f = 15 MPa with CH_4. All other experiments performed at vacuum. Hirono et al. (2019) used synthetic graphite. The same bituminous coal samples from the Brzeszcze Mine, Poland were used by Fan et al. (2020) and Liu et al. (2020). Kaneki et al. (2019) used bituminous coal samples from Ashibetsu, Japan and pure synthetic graphite.

4.1.3 Shear induced molecular change

Numerous authors who have performed friction experiments on carbonaceous materials (coal, amorphous carbon and graphite) have attributed the observed weakening to a process of strain localisation and shear induced graphitization/ordering, summarised in Figure 21. Oohashi et al. (2011) performed high velocity friction (HVF) experiments on graphite and

amorphous carbon and discovered that both samples had a similar steady state friction coefficient of 0.08 and 0.12 respectively (Figure 21). The authors suggest that the weakening trend (μ_{peak} = 0.56) in amorphous carbon is caused by frictional heating at asperity contacts which results in graphitization. However, this weakening trend has also been observed in low velocity experiments (LVF) on coal (Fan et al., 2020) and shale-coal simulated fault gouge (Liu et al., 2020) (Figure 21). These experiments were performed at 100ºC and considering the slip velocities used (1 - 100 μms^{-1}), the influence of frictional heating could be eliminated. In addition, the same displacement weakening trend was observed under vacuum and with pore fluid indicating that local over pressuring effects could be ignored (Faulkner et al. 2018). In creep experiments (P_c = 500 MPa, T = 300 – 500 ºC, $\dot{\varepsilon}$ = 1.3x10^{-6} to 1.3x10^{-4} s^{-1}) on higher rank coal than used in this study, Ross et al. (1991) found that aromatic layers, which are the basic structural units in coal, became more ordered during deformation and progressively aligned along the plane of flattening. The authors suggest that the changes are caused by shear stress which significantly reduces the activation energy for graphitization of coal. This carbonization process, which releases H^+, O^{2-} and CH_4 from the aromatic layers, occurs via the accumulation of strain energy at a given confining pressure. The study is based on the transformation from anthracite to graphite, however, the principle still applies for lower rank coals. Furthermore, the emission of functional groups (H^+, O^{2-} and CH_4) results in an increase in coal rank, see section 1.2.3 for description of molecular structure of coal. However, none of the authors who have observed shear induced ordering in LVF experiments report gas emissions (Figure 21).

The decrease in $\left(\frac{I_D}{I_G}\right)$ and increase in L_a upon shearing seen in the coal rich samples (≥50 wt% coal) in this study indicates that shearing leads to a change in molecular structure of the coal. As outlined in section 1.2.3 the molecular structure of coal evolves with increasing rank as aromatic rings are condensed forming more extensive aromatic layers. This results in a molecular structure closer to that of Graphite and reflects an increase in coal maturity (Jiang et al., 2019). Strain localisation and the accumulation of strain energy therefore provides an explanation for the observed weakening. Furthermore, this mechanism is independent of fluids so is in agreement with the findings of Fan et al. (2020) who observed the same weakening trend in vacuum dry samples. Logan et al. (1992) used a simple Finite Element method to model the development of a Riedel shear fracture array as a function of shear strain, see section 1.2.1 for description of fracture array. The authors discovered that the stress field within an experimental shear zone rotates with shear strain causing riedel shears to develop at lower angles to the gouge driver block interface. Furthermore, they note that there is likely considerable heterogeneity in both deformation and the stress field within the gouge. This means that different regions will be at different stages along the material stress-strain curve. The later conclusion is particularly relevant for shear induced molecular change in coal as the decrease in $\left(\frac{I_D}{I_G}\right)$ in sample s041 (50 wt% coal, D_{tot} = 1.949 mm) indicates molecular change will occur at relatively low macroscopic shear strains. Further to this, assuming that molecular change occurs due to accumulation of strain energy, molecular change will be focussed at asperity contact points between grains. It is plausible that as the aromatic layers become more extensive the true contact area will increase. The low friction of the graphite like structure could conceivably provide favourable sliding surfaces. This is in agreement with molecular dynamic simulations between amorphous carbon and diamond films at a rate of 10 ms^{-1} performed by Ma et al. (2014). The authors demonstrate that structural ordering and C-C

reorientation towards the direction of shear where strain localises results in shear weakening. Furthermore, the low friction is due to the clustering of graphite-like sheets and leads to stable slip. The steady state friction coefficient of ~0.23 in coal rich samples therefore represents an equilibrium crystallinity or degree of ordering of the molecular structure.

4.2 Effect of coal on velocity dependence of friction

4.2.1 Micromechanical framework of granular aggregates

Natural faults commonly contain fault gouge which governs the frictional behaviour of the fault. The frictional behaviour of the gouge is influenced by a variety of factors including grain size, mineralogy, pore fluid pressure, confining pressure, pore fluid chemistry, slip velocity and temperature. The RSF method for modelling the frictional behaviour of faults is purely phenomenological and describes the behaviour of asperities on an interface. However, mature faults that has accommodated meters of slip are composed of fault gouge which represents a shear zone of finite thickness. Hence the method does not reflect the real physical mechanisms that are controlling friction.

Microphysical models have been devised to describe the processes governing deformation in fault gouge and interpret the results of RSF modelling. The Niemeijer and Spiers (2007) model for shear deformation in granular aggregates is based on competition between rate-insensitive dilatant processes and rate-sensitive, creep processes. The authors deduced three deformation regimes shown in Figure 22. At low shear rates or sufficiently high temperatures, shear strain is accommodated by non-dilatant intergranular grain boundary sliding (GSB) via dislocation creep or diffusion creep processes. This results in frictional-viscous flow if GBS is controlled by grain boundary friction coefficient or viscous flow if GBS is non frictional. This also results in velocity strengthening (Figure 22). At higher shear rates dislocation and diffusion creep are too slow to accommodate GBS resulting in intergranular dilation and porosity generation. The competition between time dependent compaction creep and dilation due to granular flow results in steady state frictional flow (Figure 22). In this regime steady state porosity is reached resulting in velocity weakening. A third regime exists at the higher shear rates where frictional granular flow will dominate once a critical porosity is exceeded, resulting in steady critical state flow and velocity strengthening. In the following sub-sections, this three-regime model will be used to try to explain the effect of coal on the velocity dependence of friction in this study. The model is based on friction experiments on halite-muscovite gouge however the mechanisms can be applied to both single phase and multiphase gouge compositions.

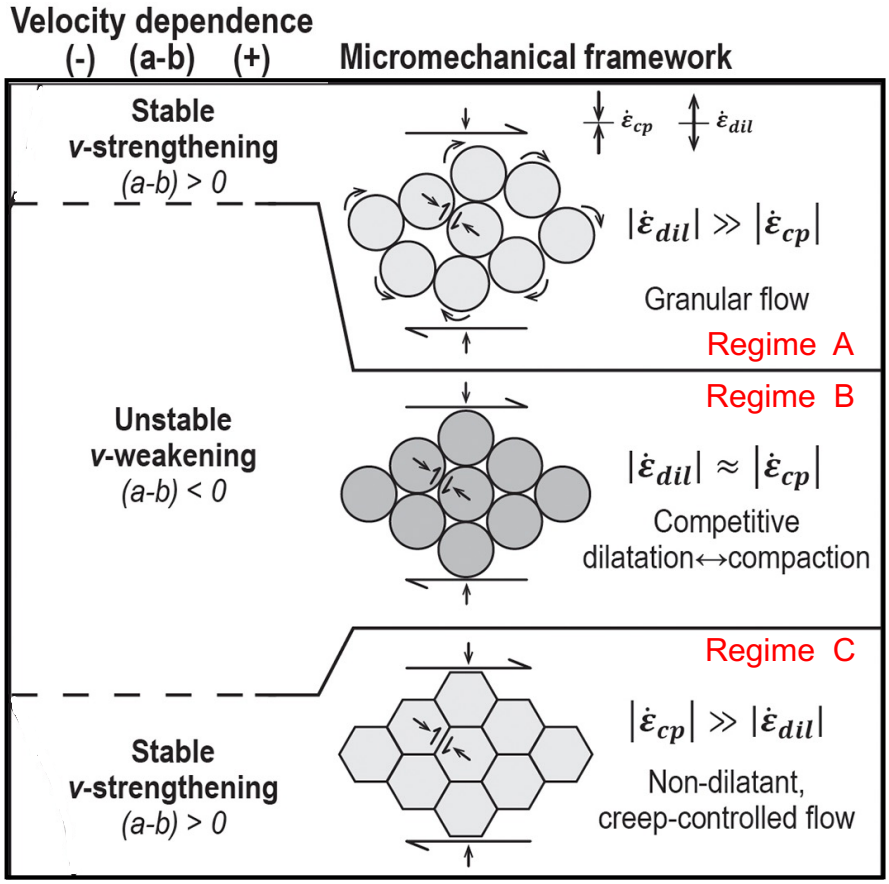

Figure 22: Microphysical framework for shear deformation of granular aggregates. Modified from Verberne et al. (2020). $\dot{\varepsilon}_{cp}$= rate of creep-controlled compaction, $\dot{\varepsilon}_{dil}$= rate of dilation by granular flow. Model framework for shear of gouge-filled faults involving competition between creep-controlled compaction and dilatation by granular flow. From bottom to top shear strain is accommodated by intergranular grain boundary sliding (GBS) by diffusion or dislocation creep processes (Regime C). At higher shear rate the competition between compaction creep and granular flow results in a steady state porosity at a given shear rate, effective normal stress and temperature which leads to velocity weakening (Regime B). At even higher shear rates the dilation rate due to frictional granular flow exceeds critical steady state porosity resulting in velocity strengthening (Regime A).

4.2.2 Coal Cliff sandstone

Velocity stepping experiments on the Coal Cliff sandstone end member indicate that it is velocity strengthening at 1 and 10 μms^{-1} (Figure 23). Rate sensitivity parameters *(a-b)* range from 0.0035 to 0.067 which are comparable with similar studies at room temperature on clay rich gouge mixtures by Ikari et al. (2009) and Tembe et al. (2010). The first evolution parameter, b1 which is close to 0 or slightly negative at 1 μms^{-1} and approximately -0.0026 at 10 μms^{-1}, has the greatest influence on *(a-b)*. In comparison *b2* is close to 0 in all velocity up-steps. Contact saturation is a possible explanation for the close to 0 *b2* values which occurs when the asperity contact area is maximised through alignment of clay minerals (Saffer and Marone, 2003; Ikari et al. 2009). Therefore, the contact area does not evolve following a velocity step resulting in b = 0. However, this cannot explain the negative b1 values. The development of kink structures composed of clay grains is an alternative explanation (Ikari et

al. 2009). If so, this will result in dilation of the gouge layer and velocity strengthening, in other words regime A in figure 22.

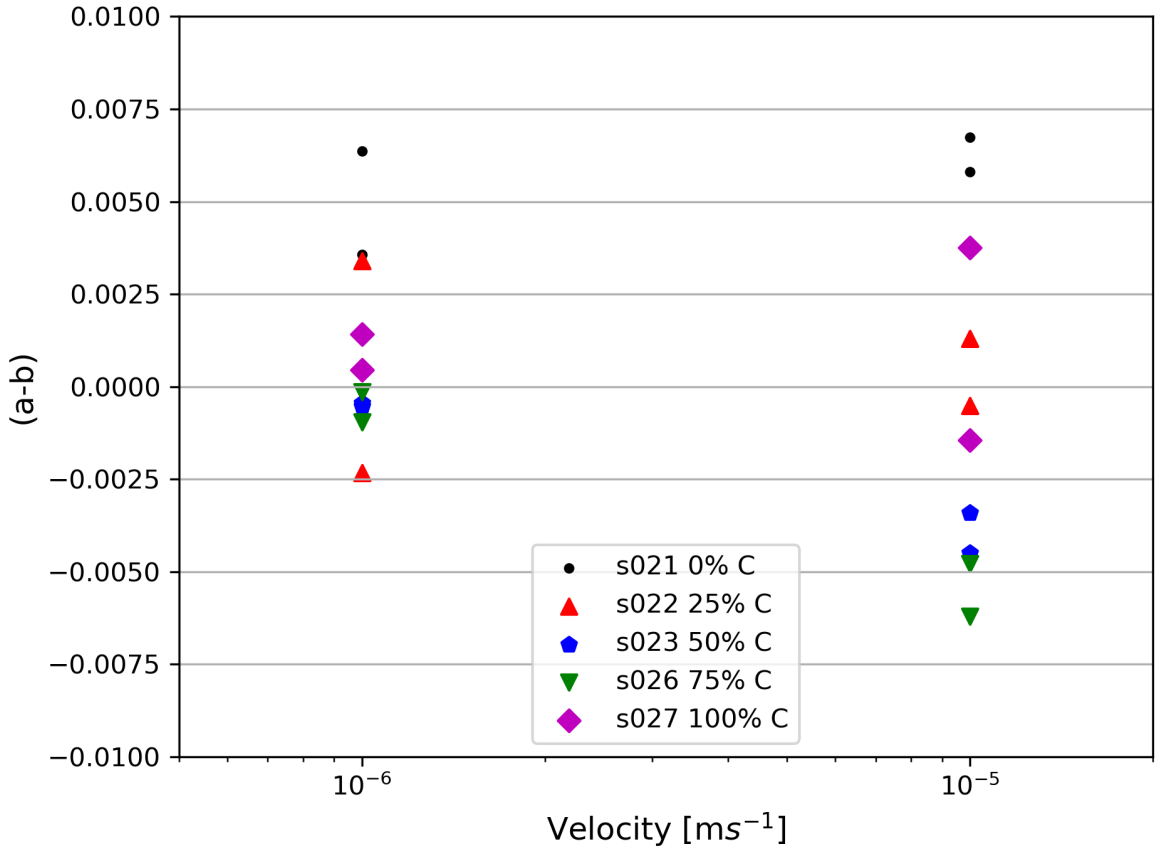

Figure 23: a-b vs slip velocity. Slip velocity is the new slip velocity in each velocity step. Positive (a-b) indicates velocity strengthening and negative (a-b) indicates velocity weakening.

4.2.3 Illawarra coal

The Illawarra coal end member was velocity strengthening in the first (0.1 - 1 μms^{-1}), third (10 - 1 μms^{-1}) and fourth (1 - 10 μms^{-1}) velocity steps although velocity weakening in the second step (1 – 10 μms^{-1}). The direct effect parameter, *a* has a consistent value of ~0.004 for all but the first velocity step indicating that the velocity dependence of asperity contact strength is constant. As discussed in section 4.1.3, the steady state strength of the gouge represents an equilibrium degree of ordering between that of graphite and amorphous carbon hence asperity contacts will have a steady state strength. In the first velocity step, a is considerably less (0.0021) although this is likely due to the stage in deformation. At this displacement the ordering of the molecular structure is still evolving as steady state has not yet been reached. At 1 μms^{-1} the coal end member is velocity neutral or slightly velocity strengthening which is characteristic of regime C (Figure 22). It is likely that at this slip velocity GBS will be controlled by the friction coefficient of grain boundaries/asperity contacts which will be low or decreasing due the molecular ordering of the coal resulting in frictional-viscous flow. It is also possible that graphite flakes may detach from the coal grains during ordering of the molecular structure and form a foliation which will promote GBS. In the first velocity up step to 10 μms^{-1} frictional-

viscous flow may be too slow and the competing effect of dilation through granular flow will lead to the observed velocity weakening (negative a-b). However, as the difference in velocity is only 1 order of magnitude it is likely that the velocity weakening is simply the impact of the displacement weakening trend, especially considering that the velocity step occurs at ~2mm of total displacement. In the final velocity step, from 1 to 10 μms^{-1} the coal has reached a steady state crystallinity. The *b2* value for this velocity step is -0.0022 however is positive in all of the other velocity steps. As outlined in the previous section an explanation for negative *b* values in clay rich gouge is the development of kink structures which result in dilation. However, as microstructure analysis of the coal end member was not possible this can only be hypothesised. Regardless the negative *b2* results in velocity strengthening. Coal also displays unique and complex swelling/shrinkage properties which will likely influence dilation and whether shear can be accommodated through frictional-viscous GBS. The swelling/shrinkage properties are controlled by the net effect of three processes: permanent compaction creep, the thermodynamic effect of a stress driven reduction in water sorption capacity of coal and stress driven closure of the transport paths (Liu et al., 2018). The water adsorption behaviour of coal is primarily controlled by heterogeneities in the coal surface caused by polar oxygen containing groups (Liu et al., 2021). Therefore, if shearing results in an increase in coal maturity, in other words, the omission of function groups between aromatic carbon rings, it is conceivable that this will also affect sorption capacity of the coal and potentially the velocity dependence of friction.

4.2.4 Mixed sandstone – coal

Sample s022 which contains 25 wt% coal displays velocity weakening in the first two velocity steps but then velocity strengthening in the third and fourth step. All of the velocity steps have a low *b1* values (~0.0008) which as explained in section 4.2.2 may indicate that asperity contacts are close to saturation i.e. contact area will not change due to the alignment of clay minerals. Parameter *b2* is the primary cause of the observed velocity weakening in the first two velocity steps and decreases with successive steps. The Raman data from the constant slide experiments containing 25 wt% coal (s042 and s040) indicated that there was no significant increase in the coal crystallinity with shear. A discontinuous B-shear was observed in samples s042 (25 wt% coal, D_{tot} = 1.5 mm) implying that strain had not yet fully localised along the boundary of the samples. Considering the displacement of the first and second velocity steps in s022 strain will not have fully localised and there will only be a discontinuous boundary shear. Hence the displacement weakening associated with strain localisation is likely the cause of the observed velocity weakening. At higher displacement, strain has localised and contact saturation will limit compaction hence gouge porosity will approach a critical state promoting velocity strengthening (regime A).

The samples with 50 wt% and 75 wt% coal show markedly different velocity dependence to either of the end members. As outlined in section 4.2.2, compaction in the coal end member is accommodated through shear enhanced ordering of the molecular structure of the coal. Shear is accommodated through frictional GBS due to the low friction of asperity contacts. Microstructural analysis of sample s031 (50 wt% coal, D_{tot} = 5.161 mm) showed that the boundary shear contained an abundance of intergranular clay minerals. With this in mind, it is unlikely that shear is accommodated by frictional GBS due to the low friction coefficient of coal-coal grain contacts. Regime C in the Niemeijer and Spiers (2007) model assumes that shear is accommodate by slip on/over a muscovite foliation and accommodated by pressure

solution of the intervening halite grains. This is based on observations of the microstructure that develops at low shear rates which displays a continuous anastomosing foliation composed of muscovite flakes. In contrast the velocity weakening regime is associated with a more chaotic microstructure. The clay content in s023 (50 wt% coal) and s026 (75 wt% coal) is ~0.22 wt% and ~0.11 wt% respectively and the foliation of the B shear in s031(50 wt% coal, D_{tot} = 5.161 mm) is only close to anastomosing in certain areas. The clay content in these samples is evidently large enough to inhibit coal-coal grain GBS however too small to form a continuous foliation resulting in a competition between compaction creep processes and dilatation through granular flow and hence velocity weakening (Regime B). It also explains why *b2* is larger at 10 μms^{-1} as increase slip velocity will promote dilation and porosity generation. This highlights that a small clay component can have a dramatic effect on the velocity dependence of coal.

4.2.5 Comparisons with previous work

Experiments by Liu et al (2020) produced comparable a-b values for their coal end member at slip velocities from 0.3 – 100 μms^{-1} as those in this study. However, they observed velocity strengthening in their 50:50 shale-coal mixture in all velocity steps. In their 25:75 shale-coal sample, velocity weakening was observed in the step from 1 to 10 $\mu ms^{-1,}$ however the gouge exhibited velocity strengthening characteristics in the 0.3 – 1 μms^{-1} and 10 – 100 μms^{-1} velocity steps. The Carboniferous shale used in their study has a similar composition to the Coal Cliff sandstone with a quartz and phyllosilicate content of 55 wt% and 35 wt%, respectively (Hunfield et al., 2017). The primary clay mineral is illite (21 wt%) which is a swelling clay, compared to kaolinite in the Coal Cliff sandstone which is non swelling. Considering the coal already experiences swelling/shrinkage effects, the mineralogy of the clay minerals will likely have an impact on the velocity dependence of coal rich samples (s023 and s026). The vitrinite reflectance value, which is a common method for classifying coal rank, quoted by Day et al. (2008) for the Illawarra coal is 0.98 compared to 0.77 for the Brezeszcze coal. This disparity combined with an observed increased crystallinity with shear of the Illawarra coal sample used in this study may be a possible cause for the considerable difference in velocity dependence. However, Liu et al. (2020) also showed that pore fluid/ gas chemistry affected the velocity dependence in 50:50 shale-coal samples so this cause cannot be eliminated. They observed velocity weakening under vacuum, CH_4 and Ag pore conditions. In addition, the effect of pore fluid composition on shear enhanced changes in the molecular structure of the coal has yet to be investigated.

4.3 Implications for seismicity in the Sydney basin and Groningen gas field

The results of the friction experiments on simulated fault gouges composed of Coal Cliff sandstone and Illawarra coal indicate that a large volume fraction of coal (≥50 wt% coal) can have a considerable impact of fault strength. The sandstone and coal end members have a similar μ_{peak} of 0.425 and 0.419, however μ_{ss} of 0.384 and 0.245, respectively. The intense post-peak displacement weakening trend in the coal end member occurs within the first ~2mm of displacement before reaching steady state. Furthermore, sandstone-coal samples containing >50% coal exhibit an almost identical displacement weakening trend as the Illawarra coal end member implying that coal dictates fault friction in the coal rich samples. A combination of microstructural analyses and Raman spectroscopy indicates that shear induced changes in molecular structure where strain localise is the primary cause of the post

peak displacement weakening trend. This process also dictates steady state friction in coal rich samples and represents an equilibrium degree of ordering of the molecular structure of coal.

When considered from a RSF perspective, both end member samples exhibit velocity strengthening (a-b>0) at 1 and 10 μms^{-1} whereas the coal rich samples (50 wt% and 75 wt% coal) are velocity weakening (a-b<0) at both velocities. When using RSF theory to assess the seismic potential of faults it is essential to consider how the lab in-situ conditions differ from the in-situ conditions of faults in nature. For example, local heterogeneity in coal rank, gas content and sorption capacity will influence the stress distribution and mechanical properties (Day et al., 2008; Hol et al., 2011). Nonetheless the results from this study indicate that there is very limited risk of earthquake nucleation on faults within each individual lithology however the interaction between the coal and other minerals in the gouge is fundamental to the velocity dependence. Sandstone hosted faults in which fault gouge has become enriched with coal may be prone to the nucleation of seismicity. Furthermore, there are numerous fault outcrops in the Sydney basin which have evidence of coal smearing such as those in the Burwood Beach fault zone (McLoughlin et al., 2021). As all experiments were performed with DI water as the pore fluid it is not possible to say whether velocity weakening will also occur under vacuum or when using other pore fluids such as brine, Argon, CO_2 or CH_4. The latter is particularly relevant as coal seams often contain large volumes of Coal Bed Methane (CMB) which will influence the frictional stability of faults. Furthermore, this is an important consideration when assessing seismic hazard not just of natural seismicity but also induced seismicity due to gas extraction or CO_2 injection (Mazzotti et al, 2009; Hol et al. 2011).

Slide-hold-slide (SHS) experiments were not performed in this study however Liu et al. (2020) performed one SHS experiment on a 50:50 shale-coal samples and observed only very minor healing/restrengthening. In addition, Fan et al. (2020) also observed only minor healing in the coal end member. Hunfield et al. (2020) demonstrated that the Carboniferous shale end member displayed almost no healing or frictional strength drop between hold periods. In contrast, the Slochteren sandstone reservoir rock showed considerable healing followed by rapid displacement weakening upon reactivation. The premise of this study was that the Coal Cliff sandstone could be used as an analogue for the Slochteren sandstone, however XRD analysis indicates that the former has a significantly larger clay content. Considering the similarities in the displacement weakening trends with those of Liu et al. (2020) it is probable that healing/restrengthening is also negligible in the samples in this study. However further experiments are required to study healing affects and how samples would respond following reactivation. As such, at this stage it is no possible to say with confidence whether coal rich faults in the Sydney basin are susceptible to reactivation and hence the potential for seismic slip.

5 Recommendations and future research

5.1 Improvements to microstructural analysis

Microstructural analysis of coal proved to be one of the most challenging aspects of the project and individual coal grains could only be identified using FIB-SEM. Furthermore, coal grains are only definable due to the presence of intergranular clays. The most suitable approach to capture coal-coal grain contacts in samples containing 100 wt% coal would be to preserve the

samples in blue epoxy. The contrast may be sufficient for grain contacts to be imaged with a light microscope. In addition, it is possible that shear enhanced ordering in the molecular structure of the coal may also result in the development of a preferred orientation in the shear bands. This could be investigated with Electron Backscatter Diffraction (EBSD) analysis.

Subject to fine tuning of the method, it would be possible to carry out friction experiments using PEEK (Polyether Ether Ketone) pistons and then use particle tracking to study the smearing mechanisms. This would also aid with interpretation of the coal rich zones observed in samples s041 (50 wt% coal, D_{tot} = 1.949 mm) and s031 (50 wt% coal, D_{tot} = 5.161 mm) (Figure 14).

5.2 Future work

The findings from this study have highlighted areas of future research that are specific to the joint University of Sydney (UoS) – Utrecht University (UU) project and more general points on the frictional properties of coal and coal rich fault gouge. Regarding the UoS – UU project, additional experiments are required using 30 wt% and 40 wt% coal to better constrain the weakening trend. In addition, it would be beneficial to perform velocity stepping experiments with 80 wt% and 90 wt% coal to study the transition from velocity weakening to strengthening. Gas zonation occurs in coal seams in the Sydney basin hence as mentioned previously it is necessary to perform additional experiments under different pore conditions.

A number of questions remain unanswered which have broader implications for the influence of coal on the frictional properties of fault gouge. Including, what influence additional weak materials have on the weakening trend and velocity dependence. In addition, the influence of load point velocity and pore fluid chemistry on shear induced molecular change remains poorly understood.

6 Conclusions

This study investigated the influence of coal on the frictional properties of the Coal Cliff sandstone to assess the potential for earthquake nucleation on faults in the Sydney basin. Velocity stepping friction experiments were performed varying coal content (wt%) and RSF parameters were derived to quantify the velocity dependence of friction. This was combined with SEM, XCT and quantitive image analysis to study the microstructural evolution of the fault gouge. Raman spectroscopy was also used to identify changes in the molecular structure of coal upon shearing. The main observations and conclusions are summarised as follows:

1. Fault gouge containing 100 wt% Coal Cliff sandstone has a μ_{peak} = 0.425 and μ_{ss} = 0.384 at P_c = 55 MPa, P_f = 15 MPa and T = 100°C using DI water as the pore fluid. Under the same conditions, 100 wt% Illawarra coal has a similar μ_{peak} of 0.419 however undergoes intense post peak displacement weakening withing the first ~2 mm of shearing before reaching a μ_{ss} = 0.245. Samples containing a mixture of coal and sandstone have a similar μ_{peak} = ~0.43 although those containing ≥50 wt% coal follow a similar weakening trend as the coal end member with μ_{ss} = ~0.23.
2. Microstructural observations of samples containing ≥50 wt% coal, show that strain localises in riedel and boundary shears which become enriched with coal.
3. Raman spectroscopy indicates that the molecular structure of coal evolves upon shearing through shear enhanced ordering which is focussed at highly strained asperity contacts where strain localises. The aromatic layers become more extensive and functional groups are omitted resulting in an increase in coal rank and molecular structure closer to that of graphite. This promotes weakening and is the primary cause of the post peak weakening trend within the first ~2mm of displacement in coal rich samples (≥50 wt% coal). Furthermore, the low steady state friction coefficient of ~0.23 represents an equilibrium degree of ordering/crystallinity resulting in stable steady state slip.
4. The Illawarra coal and Coal Cliff sandstone end members are both velocity strengthening (a-b>0) at 1 and 10 μms^{-1} however coal rich samples (≥50 wt% coal) are velocity weakening (a-b<0) at both slip velocities. Frictional-viscous GBS due to the low coefficient of coal grain contacts dominates in the Illawarra coal end member. In the Coal Cliff sandstone end member, the development of kink structures due to the high clay content results in velocity strengthening. The presence of intergranular clay in coal rich sandstone-coal samples (≥50 wt% coal) inhibits GBS between coal-coal grains promoting dilation. The competition between these processes results in velocity weakening.
5. The results indicate that under fluid saturated conditions (H_2O), sandstone hosted faults in the Sydney basin which have become enriched with coal through smearing, may be prone to earthquake nucleation. However, it is not possible to say how different pore conditions (vacuum, CO_2, CH_4, Ag) will influence the velocity dependence of the gouge. Furthermore, variations in molecular structure and rank of coal will likely have a considerable effect on the potential for earthquake nucleation.

7 Acknowledgements

I would like to thank my supervisors, André Niemeijer and Martyn Drury for their help and support throughout the project. I am also especially grateful to Chien-Cheng Hung for his help with experiments and x-ray microscopy and to Eric Hellebrand for his help with the SEM analysis. Finally, I also thank my parents who have been incredibly supportive throughout the project.

References

Al-Kahtany, K. and Al Gahtani, F., 2015. Distribution of diagenetic alterations in fluvial channel and floodplain deposits in the Triassic Narrabeen Group, southern Sydney basin, Australia. *Journal of the Geological Society of India*, 85(5), pp.591-603.

Australian Bureau of Statistics. 2021. *Australian Bureau of Statistics*.

Bamberry, W., 1991. Stratigraphy and sedimentology of the late Permian Illawarra Coal Measures, southern Sydney basin. New South Wales. *PhD. thesis, University of Wollongong (unpublished)*,.

Berg, S., Kutra, D., Kroeger, T., Straehle, C., Kausler, B., Haubold, C., Schiegg, M., Ales, J., Beier, T., Rudy, M., Eren, K., Cervantes, J., Xu, B., Beuttenmueller, F., Wolny, A., Zhang, C., Koethe, U., Hamprecht, F. and Kreshuk, A., 2019. ilastik: interactive machine learning for (bio)image analysis. *Nature Methods*, 16(12), pp.1226-1232.

Blanpied, M., Marone, C., Lockner, D., Byerlee, J. and King, D., 1998. Quantitative measure of the variation in fault rheology due to fluid-rock interactions. *Journal of Geophysical Research: Solid Earth*, 103(B5), pp.9691-9712.

Brandenburg, K. and Putz, H., n.d. *Match! - Phase Analysis using Powder Diffraction, Crystal Impact*. Kreuzherrenstr. 102, 53227 Bonn, Germany.

Buijze, L., van den Bogert, P., Wassing, B., Orlic, B. and ten Veen, J., 2017. Fault reactivation mechanisms and dynamic rupture modelling of depletion-induced seismic events in a Rotliegend gas reservoir. *Netherlands Journal of Geosciences*, 96(5), pp.s131-s148.

Burra, A., Esterle, J. and Golding, S., 2014. Horizontal stress anisotropy and effective stress as regulator of coal seam gas zonation in the Sydney Basin, Australia. *International Journal of Coal Geology*, 132, pp.103-116.

Chacón-Torres, J., Ganin, A., Rosseinsky, M. and Pichler, T., 2012. Raman response of stage-1 graphite intercalation compounds revisited. *Physical Review B*, 86(7).

Collettini, C., Niemeijer, A., Viti, C. and Marone, C., 2009. Fault zone fabric and fault weakness. *Nature*, 462(7275), pp.907-910.

Crawford, B., Faulkner, D. and Rutter, E., 2008. Strength, porosity, and permeability development during hydrostatic and shear loading of synthetic quartz-clay fault gouge. *Journal of Geophysical Research*, 113(B3).

Day, S., Duffy, G., Sakurovs, R. and Weir, S., 2008. Effect of coal properties on CO2 sorption capacity under supercritical conditions. *International Journal of Greenhouse Gas Control*, 2(3), pp.342-352.

Dieterich, J., 1979. Modeling of rock friction: 1. Experimental results and constitutive equations. *Journal of Geophysical Research*, 84(B5), p.2161.

Fakoussa, R. and Hofrichter, M., 1999. Biotechnology and microbiology of coal degradation. *Applied Microbiology and Biotechnology*, 52(1), pp.25-40.

Fan, C., Liu, J., Hunfeld, L. and Spiers, C., 2020. Frictional slip weakening and shear-enhanced crystallinity in simulated coal fault gouges at slow slip rates. *Solid Earth*, 11(4), pp.1399-1422.

Faulkner, D., Sanchez-Roa, C., Boulton, C. and den Hartog, S., 2018. Pore Fluid Pressure Development in Compacting Fault Gouge in Theory, Experiments, and Nature. *Journal of Geophysical Research: Solid Earth*, 123(1), pp.226-241.

Ferrari, A. and Robertson, J., 2000. Interpretation of Raman spectra of disordered and amorphous carbon. *Physical Review B*, 61(20), pp.14095-14107.

Fischbach, D. and Couzi, M., 1986. Temperature dependence of Raman scattering by disordered carbon materials. *Carbon*, 24(3), pp.365-369.

Ghani, M., Rajoka, M. and Akhtar, K., 2015. Investigations in fungal solubilization of coal: Mechanisms and significance. *Biotechnology and Bioprocess Engineering*, 20(4), pp.634-642.

Grevenitz, P., Carr, P. and Hutton, A., 2003. Origin, alteration and geochemical correlation of Late Permian airfall tuffs in coal measures, Sydney Basin, Australia. *International Journal of Coal Geology*, 55(1), pp.27-46.

He, X., Liu, X., Nie, B. and Song, D., 2017. FTIR and Raman spectroscopy characterization of functional groups in various rank coals. *Fuel*, 206, pp.555-563.

Hillis, R., Enever, J. and Reynolds, S., 1999. In situ stress field of eastern Australia. *Australian Journal of Earth Sciences*, 46(5), pp.813-825.

Hirono, T., Tsuda, K. and Kaneki, S., 2019. Role of Weak Materials in Earthquake Rupture Dynamics. *Scientific Reports*, 9(1).

Hol, S., Peach, C. and Spiers, C., 2011. Applied stress reduces the CO2 sorption capacity of coal. *International Journal of Coal Geology*, 85(1), pp.128-142.

Hou, Q., Han, Y., Wang, J., Dong, Y. and Pan, J., 2017. The impacts of stress on the chemical structure of coals: a mini review based on the recent development of mechanochemistry. *Science Bulletin*, 62(13), pp.965-970.

Hunfeld, L., Chen, J., Hol, S., Niemeijer, A. and Spiers, C., 2020. Healing Behavior of Simulated Fault Gouges From the Groningen Gas Field and Implications for Induced Fault Reactivation. *Journal of Geophysical Research: Solid Earth*, 125(7).

Hunfeld, L., Niemeijer, A. and Spiers, C., 2017. Frictional Properties of Simulated Fault Gouges from the Seismogenic Groningen Gas Field Under in situ P-T-Chemical Conditions. *Journal of Geophysical Research: Solid Earth*, 122(11), pp.8969-8989.

Jiang, J., Yang, W., Cheng, Y., Liu, Z., Zhang, Q. and Zhao, K., 2019. Molecular structure characterization of middle-high rank coal via XRD, Raman and FTIR spectroscopy: Implications for coalification. *Fuel*, 239, pp.559-572.

Jones, J., Conaghan, P. and McDonnell, K., 1987. Coal measures of an orogenic recess: Late Permian Sydney Basin, Australia. *Palaeogeography, Palaeoclimatology, Palaeoecology*, 58(3-4), pp.203-219.

Kaneki, S. and Hirono, T., 2019. Diagenetic and shear-induced transitions of frictional strength of carbon-bearing faults and their implications for earthquake rupture dynamics in subduction zones. *Scientific Reports*, 9(1).

Kortekaas, M. and Jaarsma, B., 2017. Improved definition of faults in the Groningen field using seismic attributes. *Netherlands Journal of Geosciences*, 96(5), pp.s71-s85.

Liu, A., Liu, S., Liu, P. and Wang, K., 2021. Water sorption on coal: effects of oxygen-containing function groups and pore structure. *International Journal of Coal Science & Technology*,.

Liu, J., Fokker, P., Peach, C. and Spiers, C., 2018. Applied stress reduces swelling of coal induced by adsorption of water. *Geomechanics for Energy and the Environment*, 16, pp.45-63.

Logan, J., Dengo, C., Higgs, N. and Wang, Z., 1992. Chapter 2 Fabrics of Experimental Fault Zones: Their Development and Relationship to Mechanical Behavior. *International Geophysics*, pp.33-67.

Logan, J., Friedman, M., Higgs, N., Dengo, C. and Shimamoto, T., 1979. Experimental studies of simulated gouge and their application to studies of natural fault zones. *Proceedings of Conference VIII on Analysis of Actual Fault Zones in Bedrock: US Geological Survey Open-File Report*, pp.79-1239.

Ma, T., Wang, L., Hu, Y., Li, X. and Wang, H., 2014. A shear localization mechanism for lubricity of amorphous carbon materials. *Scientific Reports*, 4(1).

Mandl, G., Jong, L. and Maltha, A., 1977. Shear zones in granular material. *Rock Mechanics*, 9(2-3), pp.95-144.

Marone, C. and Scholz, C., 1989. Particle-size distribution and microstructures within simulated fault gouge. *Journal of Structural Geology*, 11(7), pp.799-814.

Marone, C., 1998. Laboratory-derived friction laws and their application to seismic faulting. *Annual Review of Earth and Planetary Sciences*, 26(1), pp.643-696.

Mathews, J. and Chaffee, A., 2012. The molecular representations of coal – A review. *Fuel*, 96, pp.1-14.

Mazzotti, M., Pini, R. and Storti, G., 2009. Enhanced coalbed methane recovery. *The Journal of Supercritical Fluids*, 47(3), pp.619-627.

McLoughlin, S., Nicoll, R., Crowley, J., Vajda, V., Mays, C., Fielding, C., Frank, T., Wheeler, A. and Bocking, M., 2021. Age and Paleoenvironmental Significance of the Frazer Beach Member—A New Lithostratigraphic Unit Overlying the End-Permian Extinction Horizon in the Sydney Basin, Australia. *Frontiers in Earth Science*, 8.

Memarian, H. and Fergusson, C., 2003. Multiple fracture sets in the southeastern Permian-Triassic Sydney Basin, New South Wales. *Australian Journal of Earth Sciences*, 50(1), pp.49-61.

Moore, D. and Rymer, M., 2007. Talc-bearing serpentinite and the creeping section of the San Andreas fault. *Nature*, 448(7155), pp.795-797.

Mosser, L., Dubrule, O. and Blunt, M., 2017. Reconstruction of three-dimensional porous media using generative adversarial neural networks. *Physical Review E*, 96(4).

NAM, 2013. Technical addendum to the Winningsplan Groningen 2013 subsidence, induced earthquakes and seismic hazard analysis in the Groningen field.

Niemeijer, A. and Spiers, C., 2007. A microphysical model for strong velocity weakening in phyllosilicate-bearing fault gouges. *Journal of Geophysical Research*, 112(B10).

Niemeijer, A., Marone, C. and Elsworth, D., 2010. Frictional strength and strain weakening in simulated fault gouge: Competition between geometrical weakening and chemical strengthening. *Journal of Geophysical Research*, 115(B10).

Och, D., Offler, R., Zwingmann, H., Braybrooke, J. and Graham, I., 2009. Timing of brittle faulting and thermal events, Sydney region: association with the early stages of extension of East Gondwana. *Australian Journal of Earth Sciences*, 56(7), pp.873-887.

Oohashi, K., Hirose, T. and Shimamoto, T., 2011. Shear-induced graphitization of carbonaceous materials during seismic fault motion: Experiments and possible implications for fault mechanics. *Journal of Structural Geology*, 33(6), pp.1122-1134.

Oohashi, K., Hirose, T., Kobayashi, K. and Shimamoto, T., 2012. The occurrence of graphite-bearing fault rocks in the Atotsugawa fault system, Japan: Origins and implications for fault creep. *Journal of Structural Geology*, 38, pp.39-50.

PEACOCK, D. and SANDERSON, D., 1992. Effects of layering and anisotropy on fault geometry. *Journal of the Geological Society*, 149(5), pp.793-802.

Pimenta, M., Dresselhaus, G., Dresselhaus, M., Cançado, L., Jorio, A. and Saito, R., 2007. Studying disorder in graphite-based systems by Raman spectroscopy. *Phys. Chem. Chem. Phys.*, 9(11), pp.1276-1290.

Quinn, C., Glen, R. and Diessel, C., 2008. Discussion of “Geomechanical modeling of the nucleation process of Australia's 1989 M5.6 Newcastle earthquake” by C.D. Klose [Earth Planet. Sci. Lett. 256 (2007) 547–553]. *Earth and Planetary Science Letters*, 269(1-2), pp.296-302.

Rajabi, M., Tingay, M. and Heidbach, O., 2016. The present-day stress field of New South Wales, Australia. *Australian Journal of Earth Sciences*, 63(1), pp.1-21.

Ross, J., Bustin, R. and Rouzaud, J., 1991. Graphitization of high rank coals—the role of shear strain: experimental considerations. *Organic Geochemistry*, 17(5), pp.585-596.

Ruina, A., 1983. Slip instability and state variable friction laws. *Journal of Geophysical Research: Solid Earth*, 88(B12), pp.10359-10370.

Rutter, E., Hackston, A., Yeatman, E., Brodie, K., Mecklenburgh, J. and May, S., 2013. Reduction of friction on geological faults by weak-phase smearing. *Journal of Structural Geology*, 51, pp.52-60.

Rynn, J., Brennan, E., Hughes, P., Pedersen, I. and Stuart, H., 1992. The 1989 Newcastle, Australia, earthquake. *Bulletin of the New Zealand Society for Earthquake Engineering*, 25(2), pp.77-144.

Sadezky, A., Muckenhuber, H., Grothe, H., Niessner, R. and Pöschl, U., 2005. Raman microspectroscopy of soot and related carbonaceous materials: Spectral analysis and structural information. *Carbon*, 43(8), pp.1731-1742.

Saffer, D. and Marone, C., 2003. Comparison of smectite- and illite-rich gouge frictional properties: application to the updip limit of the seismogenic zone along subduction megathrusts. *Earth and Planetary Science Letters*, 215(1-2), pp.219-235.

Schindelin, J., Arganda-Carreras, I., Frise, E., Kaynig, V., Longair, M., Pietzsch, T., Preibisch, S., Rueden, C., Saalfeld, S., Schmid, B., Tinevez, J., White, D., Hartenstein, V., Eliceiri, K., Tomancak, P. and Cardona, A., 2012. Fiji: an open-source platform for biological-image analysis. *Nature Methods*, 9(7), pp.676-682.

Schleicher, A., Sutherland, R., Townend, J., Toy, V. and van der Pluijm, B., 2015. Clay mineral formation and fabric development in the DFDP-1B borehole, central Alpine Fault, New Zealand. *New Zealand Journal of Geology and Geophysics*, 58(1), pp.13-21.

Scholz, C., 2019. *The mechanics of earthquakes and faulting*. 3rd ed. Cambridge: Cambridge University Press.

Takahashi, M., Mizoguchi, K., Kitamura, K. and Masuda, K., 2007. Effects of clay content on the frictional strength and fluid transport property of faults. *Journal of Geophysical Research*, 112(B8).

Tanner, D. and Brandes, C., 2020. *Understanding faults*. Amsterdam: Elsevier.

Tchalenko, J., 1970. Similarities between Shear Zones of Different Magnitudes. *Geological Society of America Bulletin*, 81(6), p.1625.

Tembe, S., Lockner, D. and Wong, T., 2010. Effect of clay content and mineralogy on frictional sliding behavior of simulated gouges: Binary and ternary mixtures of quartz, illite, and montmorillonite. *Journal of Geophysical Research*, 115(B3).

Trusovas, R., Račiukaitis, G., Niaura, G., Barkauskas, J., Valušis, G. and Pauliukaite, R., 2015. Recent Advances in Laser Utilization in the Chemical Modification of Graphene Oxide and Its Applications. *Advanced Optical Materials*, 4(1), pp.37-65.

van den Ende, M., Chen, J., Ampuero, J. and Niemeijer, A., 2018. A comparison between rate-and-state friction and microphysical models, based on numerical simulations of fault slip. *Tectonophysics*, 733, pp.273-295.

van Thienen-Visser, K. and Breunese, J., 2015. Induced seismicity of the Groningen gas field: History and recent developments. *The Leading Edge*, 34(6), pp.664-671.

Verberne, B., Spiers, C., Niemeijer, A., De Bresser, J., De Winter, D. and Plümper, O., 2013. Frictional Properties and Microstructure of Calcite-Rich Fault Gouges Sheared at Sub-Seismic Sliding Velocities. *Pure and Applied Geophysics*, 171(10), pp.2617-2640.

Verberne, B., van den Ende, M., Chen, J., Niemeijer, A. and Spiers, C., 2020. The physics of fault friction: insights from experiments on simulated gouges at low shearing velocities. *Solid Earth*, 11(6), pp.2075-2095.

Wojdyr, M., 2010. Fityk: a general-purpose peak fitting program. *Journal of Applied Crystallography*, 43(5), pp.1126-1128.

Zhao, L., Ward, C., French, D. and Graham, I., 2013. Mineralogy and major-element geochemistry of the lower Permian Greta Seam, Sydney Basin, Australia. *Australian Journal of Earth Sciences*, 61(3), pp.375-394.

Zhao, S. and Müller, D., 2001. The tectonic stress field in eastern Australia. *Petroleum Exploration Society of Australia, Special Publication*, pp.61-70.

Appendices

A – Coal Cliff sandstone XRD

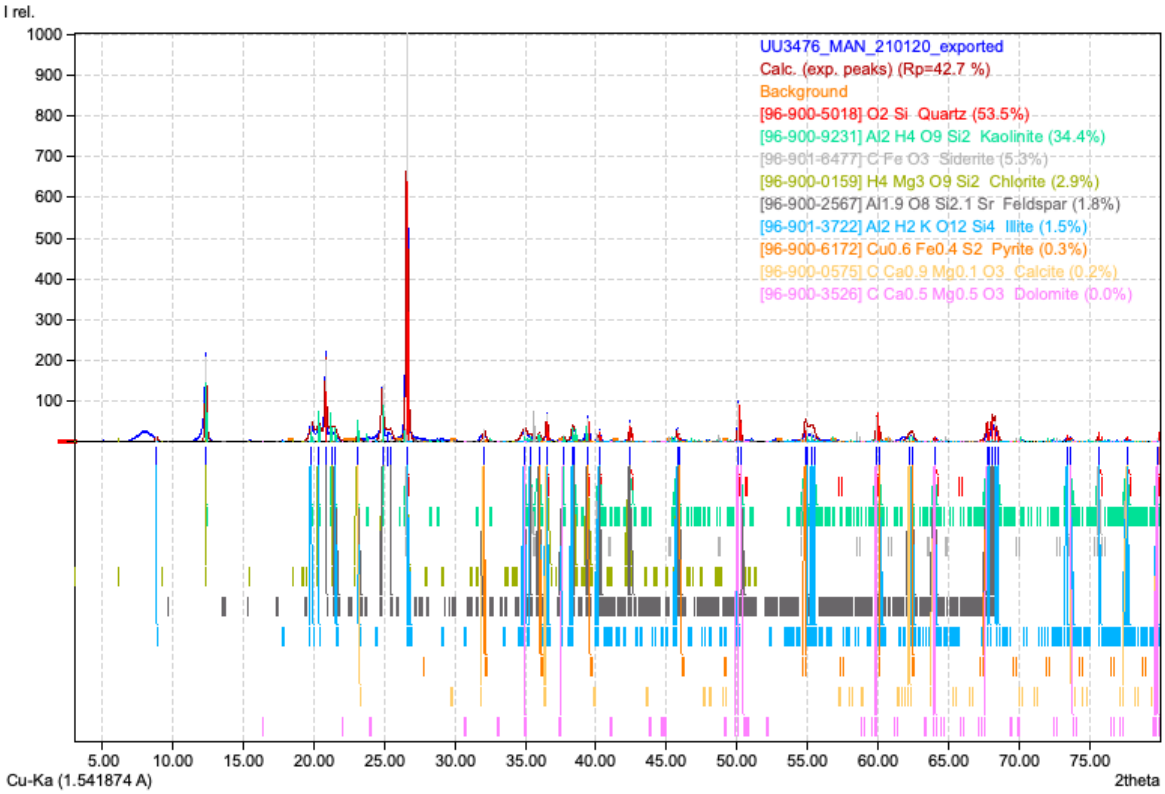

Figure A1: Results of XRD analysis of Coal Cliff sandstone sample used in friction experiments. Peak fitting was performed using Match! software (Brandenburg and Putz, n.d.).

B – Raman spectra

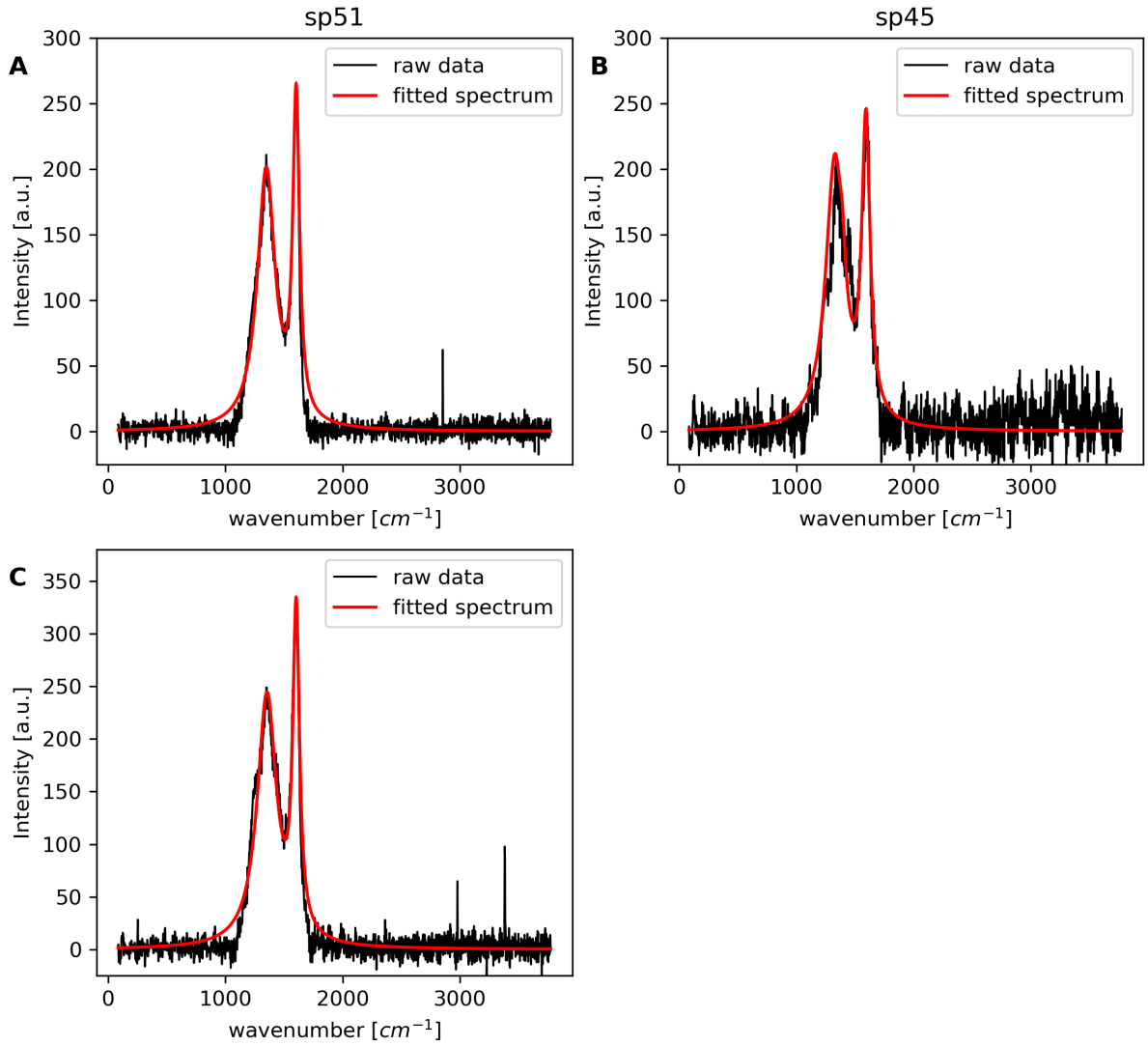

Figure B1: Raman spectra of s0XX (100 wt% coal, D_{tot} = 0). Spectra obtained at three randomly chosen locations within the sample.

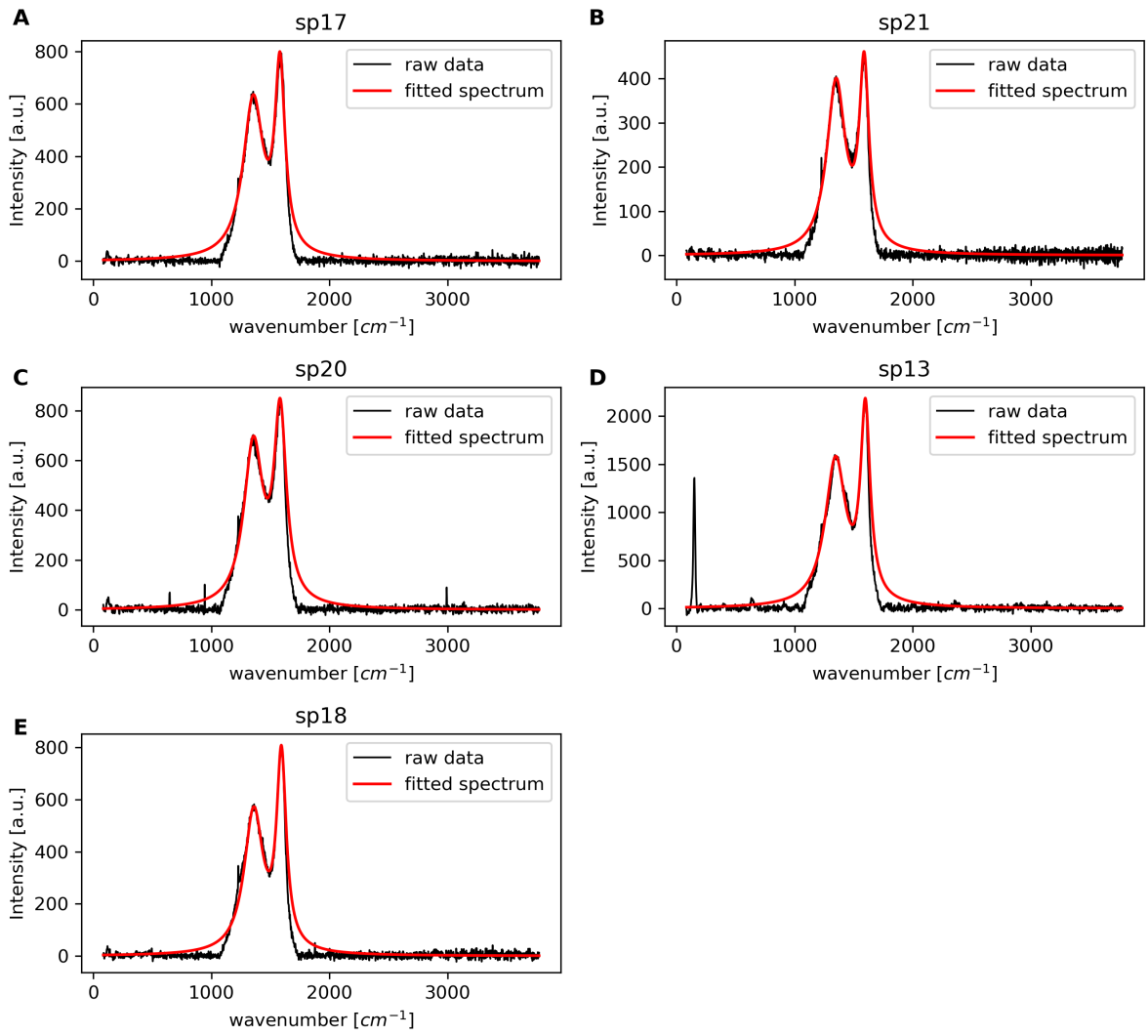

Figure B2: Raman spectra of coal in s042 (25 wt% coal, D_{tot} = 1.5 mm). (a-c) B-shear. (d & e) Matrix.

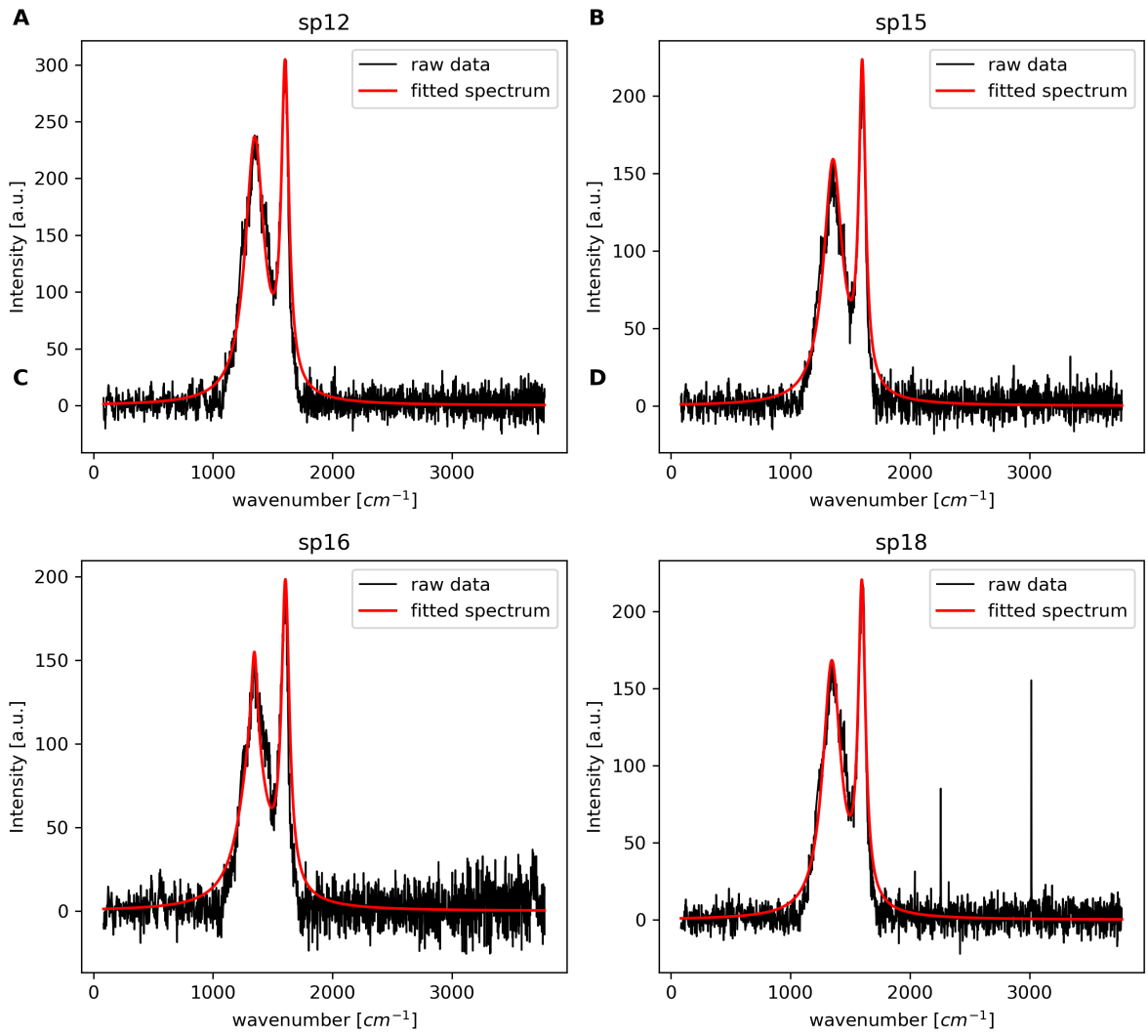

Figure B3: Raman spectra of coal in s040 (25 wt% coal, D_{tot} = 4.919 mm). (a & b) B-shear. (c & d) Matrix.

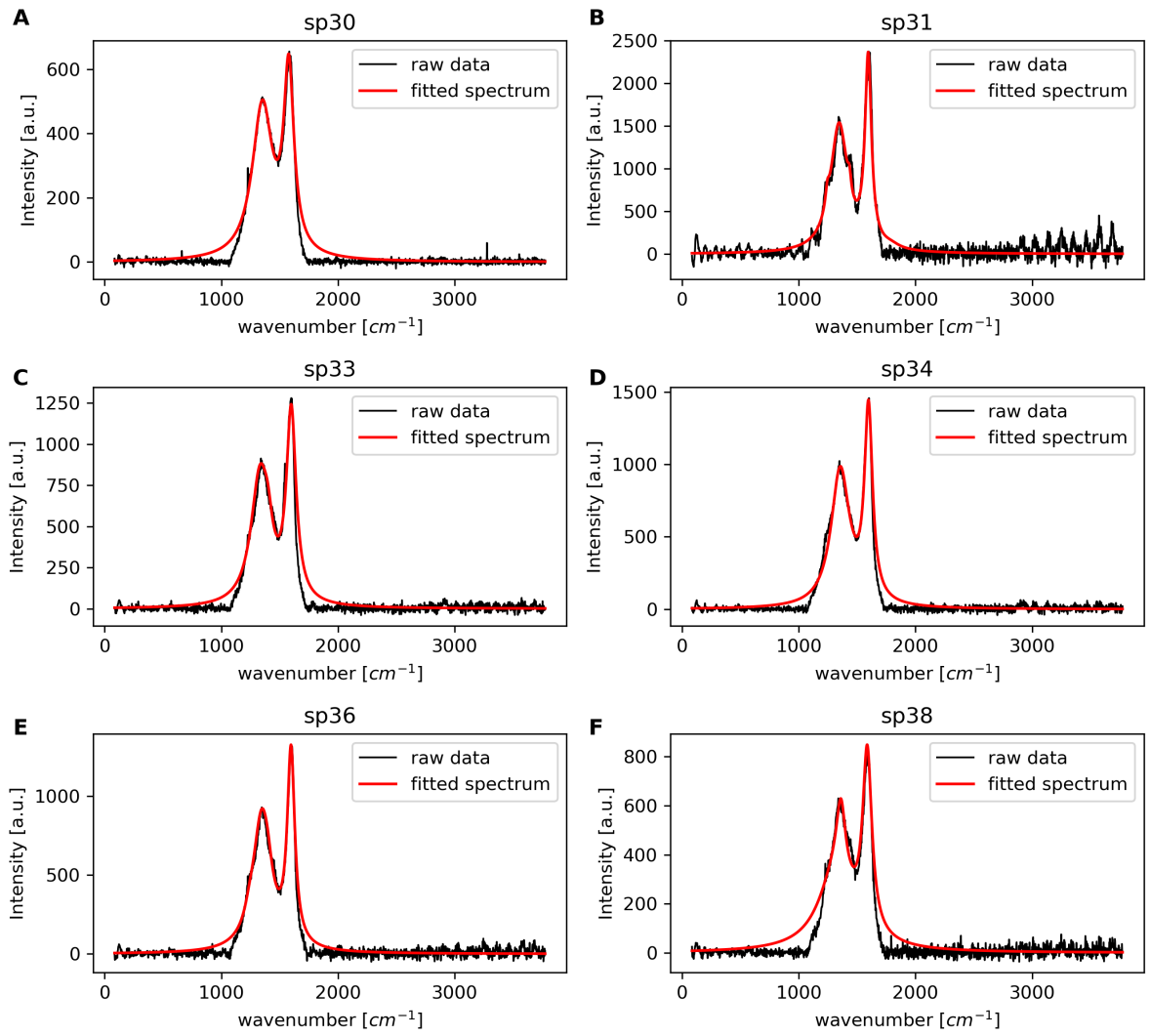

Figure B4: Raman spectra of coal in s041 (50 wt% coal, D_{tot} = 1.948 mm). (a-c) B-shear. (d-f) Matrix.

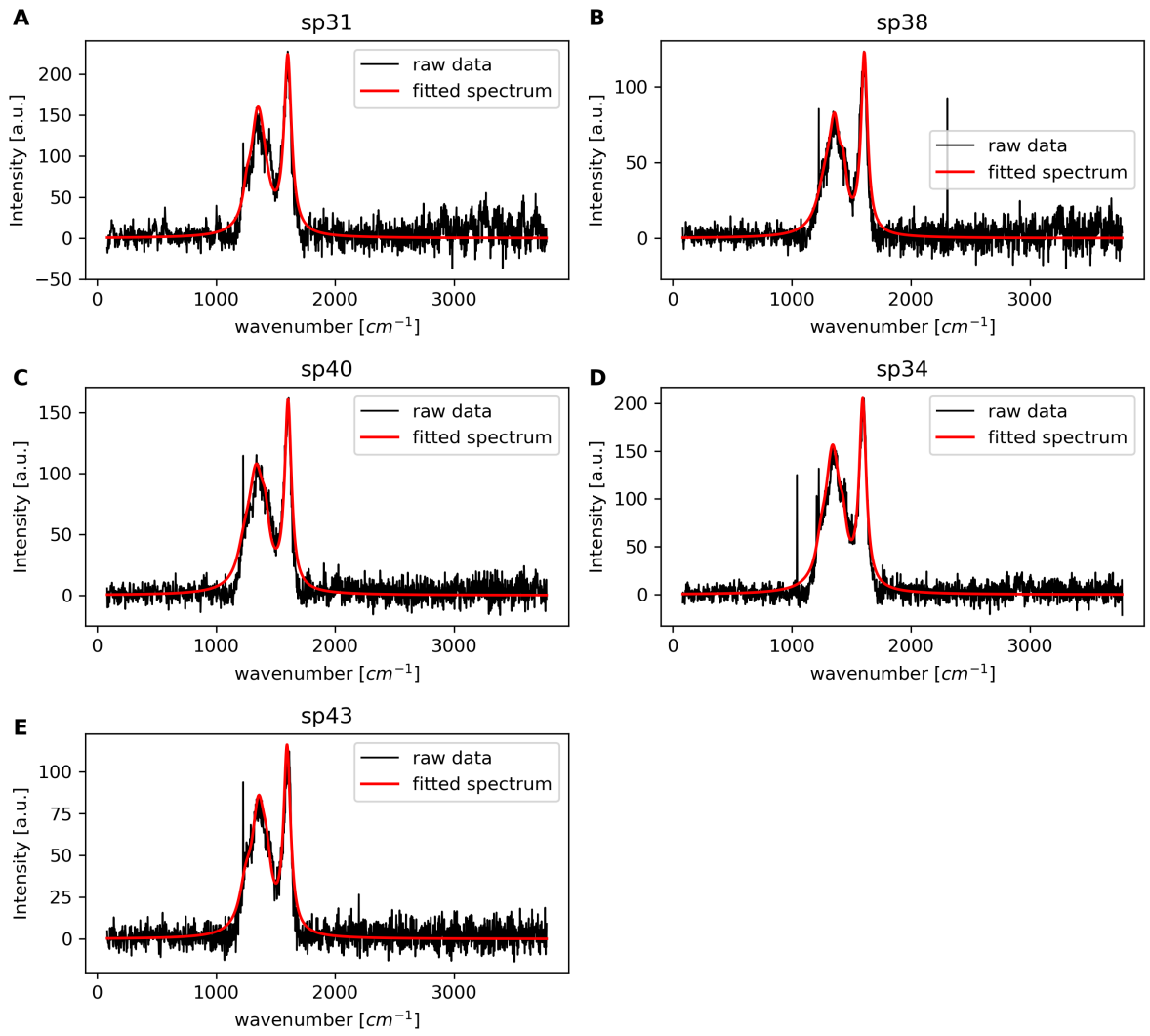

Figure B5: Raman spectra of coal in s031 (50 wt% coal, D_{tot} = 5.161 mm). (a-c) B-shear. (d & e) Matrix.